SLAC-PUB-3337
May 1984
(N)

SPIN POLARIZED ANGLE–RESOLVED PHOTOEMISSION STUDY OF THE ELECTRONIC STRUCTURE OF FE(100) AS FUNCTION OF TEMPERATURE*

E. KISKER,† K. SCHRÖDER, W. GUDAT, AND M. CAMPAGNA

Institut für Festkörperforschung der Kernforschungsanlage Jülich

Postfach 1913, D-5170 Jülich, West Germany

Abstract

By spin- and angle-resolved photoemission with synchrotron radiation the electronic structure of Fe(100) has been tested between room temperature and the Curie temperature T_c for photon energies in the range 20-70 eV. The spin-resolved energy distribution curves (SREDCs) reflect the dispersions of the $\Delta_5^{\uparrow,\downarrow}$-symmetry initial state bands. This manifests in an abrupt change in spin character of the peak near E_F from predominantly minority spin to majority spin when tuning the photon energy across 33 eV. The non-spin-resolved EDCs thereby remain nearly unchanged. Upon heating to 0.85 T/T_c, depending on photon energy, qualitative different changes in the SREDCs are observed: At $h\nu = 60$ eV, $\Gamma_{25}'^{\uparrow}$ is found to be stationary in energy upon heating, and the spin-summed intensity decreases less than 5%. $\Gamma_{25}'^{\downarrow}$ becomes strongly broadened in energy and wave vector, resulting in a strong loss of intensity. Contrary, at $h\nu = 31$ and 21 eV, an increase in minority-spin (and total) photocurrent upon heating is observed. This is interpreted as resulting from a decrease of the exchange splitting with temperature near H.

Submitted to Physical Review B

PACS: 75.50.Bb, 75.10.Lp, 79.60.Ch

---

* Work supported by the Department of Energy, contract DE-AC03-76SF00515.

† On sabbatical leave to Stanford Linear Accelerator Center, Stanford University, Stanford, CA 94305.

1. Introduction

The electronic structure at finite temperatures of the 3d-transition metals Fe, Co and Ni is currently a matter of strong theoretical interest. One of the problems is to calculate the Curie temperature (T_c), which is known to be much smaller than estimated from the magnitude of the ferromagnetic exchange splitting. This is contrasted by the fact that spin-polarized band theory based on the self-consistent local density functional description gives an adequate account of the ferromagnetic ground state (e.g. cohesive energy, non-integral moments).[1] The basic common idea behind present theories is to allow for the existence of local magnetic moments even above T_c.[2–6] The ferromagnetic to paramagnetic phase transition is then governed by thermal disordering of the moments, requiring much less energy than single-particle spin-flips which would involve energy changes as large as the exchange splitting. The controversy is on the spatial extent of correlation among the magnetic moments, which is connected intimately to the present debate on the existence of spin waves above T_c.[7,8]

It has been pointed out recently that a strong indication for the persistence of unchanged local moments to temperatures above T_c is found in the magnetovolume effect of Fe and Ni.[9] I.e., it is the absence of a strong lattice contraction, which, from band theory, is expected to occur with the loss of spontaneous magnetization.[1] This, on the first sight, would be regarded as support of present theories which involve local magnetic moments. However, magnetovolume-effect together with specific heat data infer that the magnetic moment does not change at all between $T = 0$ and above T_c.[9] This, for Ni, is in contradiction to any calculation which predict a decrease of the magnetic moment of at least 25% between $T = 0$ and $T = T_c$. No explanation for this fundamental discrepancy is known.[9]

Since photoemission, and especially angle-resolved photoemission, from clean single crystals, probes the electronic structure in a rather direct way, it has been tried in many works to observe changes in the spectra when heating the sample to T_c, and higher.[10,11] Although the electron spin has not been measured in

these experiments, exchange-split states have been identified, and a decrease of the exchange splitting up to $T/T_c = 0.94$ of about 20% has been inferred. However, only by measuring actually the electron spin, exchange split bands can be identified unambiguously and the band dispersions can be detected for Fe(100), as will be shown below. Furthermore, the spin dynamics at elevated temperatures, as spin rotations around the spontaneous magnetization direction or flips of local magnetic moments which currently are considered to be the driving force for the ferromagnetic to paramagnetic phase transition, can only be observed by this method. The present work[12] shows also that the primary photocurrent (as distinguished from the inelastic contribution) might not be conserved upon heating in an angle-resolved experiment due to an initial-state (and binding-energy) dependent broadening of the photoemission cone. The new data on Fe, furthermore, show for the first time experimentally that the temperature-induced changes in the energy distribution curves depend on the initial state wave vector.

2. The Timescale of the Experiment

The result of an experiment on ferromagnets depends on the probing time.[13] Phenomenologically, the physical processes occuring at finite temperatures might be characterized by two different timescales.[13,5] Electron hopping times are of the order of $h/W = 10^{-15}$ sec, where W is the bandwidth. On this timescale the formation of magnetic moments occurs also. The magnetic configuration then fluctuates on a timescale of the order of spin wave frequencies, which is typically of order $h/0.05$ eV $= 10^{-13}$ sec. On the photoelectron probing time is little information available at present. We may estimate it from the width of the states as observed in the experiment, which varies from 0.6 eV slightly below E_F to about 2 eV at 3 eV binding energy for Fe.[14] This yields lifetimes of the order of 10^{-14} sec. Hence the photoemission probing time is expected to be intermediate between the electron hopping time and the spin fluctuation time. The experiment will therefore depict a temporary image of the microscopic magnetic configuration, averaged over all configurations which occur during the long measuring time within the spatial extent of the light spot at the sample. We note

that a similar average is calculated in recent theories based on the disordered-local-moment (DLM) picture for ferromagnetism at finite temperatures.[5]

3. Apparatus and Experimental Details

3.1 Light Optics

The experiment is similar to a recent one on Ni(110)[15] in which a resonance lamp was employed. However, for being able to follow the band dispersions, we used monochromatized, tunable synchrotron radiation from the new German storage ring BESSY at W. Berlin. To accomplish most simple experimental conditions, the optical/electron-optical system was designed to use s-polarized (normal incident) light. The beamline consisted of a first mirror which focused the synchrotron radiation onto the entrance slit of the toroidal grating monochromator. The latter has been described in detail elsewhere.[16] By means of an additional mirror, the monochromatized light emerging from the exit slit was imaged onto the sample, after being bent to the electron optical axis by means of a plane mirror (see Fig. 1). The light spot size on the sample was smaller than 0.5 mm^2, matching closely the electron spectrometer acceptance. In order to be able to compensate for the uncertainty in the position of the light spot on the sample after changes in the BESSY beam optics, the mirror angle (see Fig. 1) with respect to the electron optical axis was made adjustable by means of a linear-motion feedthrough under operating conditions.

3.2 Characteristics of the Electron Spectrometer

The photoelectron spectrometer was based on a 90° spherical condensor of 15 mm mean radius. Total energy resolution, including the linewidth of the light was 0.4 eV at hv = 60 eV decreasing to about 0.25 eV at hv = 21 eV. The angular acceptance was confined to normal emission with a geometrical limitation at the source of ±6°. Further restrictions were obtained electron-optically inside of the electron spectrometer. Those depend on the electron energy since the trajectories achieve larger distances from the axis when the starting energy is larger.[17] The effective angular acceptance is estimated to be smaller than ±3°

at 60 eV and $\pm 5°$ at 20 eV. Changes in the width of the photoelectron emission cone could be detected by sweeping the electron beam across the entrance slit of the energy analyzer. Since, for optimal beam transmission, the emitting area is imaged onto this aperture, an increase in the width of the image occurs due to spherical aberrations. We note that due to the well-defined electron-optical conditions, virtually no stray electrons from apertures insides the spectrometer were detected although several lens elements were hit by stray light.

The energy distribution curves were scanned by applying a ramp voltage to the photocathode. This has the advantage that the electron-optical focusing conditions are kept unchanged when electrons with different binding (starting) energies are selected.[17]

3.3 SPIN-ANALYSIS

The spin polarization was measured by means of a Mott detector after accelerating the angle- and energy- selected electrons to 100 keV. For determining the spin sensitivity, two gold foil targets of about 3000 and 500 Å thickness, were employed. The targets were mounted on a motor-operated linear motion feedthough for selectively putting them into the beam path. The electrons were detected by surface-barrier detectors, and the preamplified pulses were decoupled from the high voltage by means of fiber-optic transmitters. The detector acceptance angle was confined to an opening angle of 0.4 (radians). Using the thicker gold foil, the count rate in the polarization-sensitive detectors was 10^{-3} times the count rate as measured by a detector in the direct beam path after removing the gold target. Count rates as high as 250/s in the polarization sensitive detectors have been obtained after 250 mA BESSY beam injection with the so-called Metro-optics in the d-band peak at 60 eV photon energy.

3.4 THE ELECTRONIC CONTROL

The photoelectron spectrometer was controlled by a microcomputer (CBM 8032),[18] which steered most of the spectrometer lens and deflection voltages via digital to analog converters (totally 28). The energy distribution curves (EDCs) were accumulated in the multiscaling mode. For each voltage step which was

output by the microcomputer when measuring the EDCs, four counters were read out and stored by the microcomputer. Three of these counters were connected to electron detectors in the spin analyzer. Two of them (under $\pm 120^o$ scattering angle) served as spin analyzers. The third detector was employed for monitoring the beam transmitted through the gold target foil. The gold foil could be removed from the beam path to obtain the spin-averaged EDC with better statistics than from the sum of the left and right detectors and also to obtain a signal with good statistics when computer-optimizing the electron spectrometer.[18] The fourth channel was used to monitor the photon flux during the measurements. This signal was derived from the total photocurrent of the refocusing mirror behind the exit slit of the optical monochromator by means of a voltage-to-frequency converter. During data acquisition, the data could be transferred to a second microcomputer (Commodore C64) which provided on-line display of the data. The spin-resolved EDCs (SREDCs) were calculated there and divided by the contents of the photon flux channels. This served for correcting the data for the steady (and sometimes discontinuous) decrease of the BESSY photon flux and enabled detection of relative intensity changes in the SREDCs occuring when the sample was heated.

3.5 The Fe(100) Sample

The sample was shaped as a thin disk of 0.4 mm thickness and 6 mm diameter, and had been spark-eroded from a high-purity single-crystal of bcc Fe. It was mechanically polished and cleaned in situ by standard surface analysis techniques. Its surface conditions were monitored by LEED and photoelectron spectroscopy at photon energies below 30 eV, where the most common surface contaminants S, C, N, O have large cross sections at binding energies between 4-6 eV.[19] The sample was mounted with the easy magnetization direction (001) parallel to the spin polarization sensitive axis of the Mott (spin) analyzer and was magnetized in this direction. The sample could be heated by radiative heating from a bifilar wound tungsten filament from the back side. A tungsten sheet served for heat reflection. The temperature was measured by means of a thermocouple, spotwelded to sample.

Prior to the measurements, the clean sample was annealed for two minutes at 800°K, and after being allowed to cool, it was transferred into a small internal magnetizing coil and magnetizing current pulses were applied. Then the room temperature measurements were performed, preferably after new BESSY beam injection to assure shortest measuring times. A measuring time less than 20 min. was chosen generally for taking the SREDCs. Then the sample was heated, and the elevated temperature EDCs taken subsequently. Spin-averaged EDCs could be taken in about 2 minutes with the Gold target foil removed from the beam path in the Mott detector. The temperature-induced intensity changes in the SREDCs which are reported below have been confirmed by comparing with the more rapidly measured spin-averaged EDCs. Further checks have been made by repeating the measurements after allowing the sample to cool down.

3.6 Spin Resolved Energy Distribution Curves (SREDCs)

From the left and right count rates I_1 and I_2 of the Mott detector, corrected for the apparatus asymmetry as determined from a measurement with a nonmagnetic target ($I_2 = I_1 \cdot 0.891$ for unpolarized electrons), the spin-resolved energy distribution curves (SREDCs) $I^{\uparrow}$ (E) and $I^{\downarrow}$ (E) are obtained as

$$I^{\uparrow,\downarrow} = 0.5\left[I \pm \frac{I_1 - I_2}{S_{eff}}\right] \qquad (1)$$

S_{eff} is the value of the foil-thickness corrected Sherman-function and I is the spin summed count rate. As mentioned above, the SREDCs are normalized to the light intensity at any selected photon energy to detect the transfer of electrons of one spin state into the other one occuring at elevated temperatures.

We note that the spin is measured in the laboratory frame, and $\uparrow$ refers to electrons with their magnetic moments parallel to the spontaneous magnetization direction. This labelling, at low temperature, is consistent with the labelling used previously in angle-resolved photemission. At elevated temperatures, angle-resolved photoemission data implicitly have refered their spin labelling to the temporary direction of a hypothetical local magnetization, which might fluctuate in time and space. Our spin-resolved data are also at elevated temperatures

refered to the spontaneous magnetization direction, which remains fixed below T_c.

3.7 Temperature Effects on the Spin Polarization

Due to the loss of spontaneous magnetization above T_c, SREDCs become equal at and above T_c. The information on the changes in the microscopic electronic structure is contained in the way they approach each other. This might occur principally in two ways: i) When the exchange splitting is reduced at elevated temperature purely by Stoner-like band-shifts, this will result in shifts of the exchange split peaks in the SREDCs until the peak positions become equal at $T = T_c$. Simultaneously, the spin-summed EDC becomes narrower due to the line shifts. ii) When constant magnetic moments tend to precess due to thermal disorder under angle θ with respect to the spontaneous magnetization direction, this will result in a balancing of losses in one spin state and gains of the other one. This is because an electron in pure spin state with respect to a hypothetical local magnetization direction will be detected with probability $\cos^2\theta/2$ in one channel of the spin analyzer and with probability $\sin^2\theta/2$ in the other one. The spin-summed EDC would remain unchanged if the rotation is the only effect since $\sin^2\theta/2 + \cos^2\theta/2 = 1$. The rotation includes also the special case $\theta = 180^o$ corresponding to alternating magnetic moments.

From the spin resolved intensities $I^\uparrow$ and $I^\downarrow$, the spin polarization can be calculated as $P = (I^\uparrow - I^\downarrow)/(I^\uparrow + I^\downarrow)$ and $I^{\uparrow,\downarrow} = 0.5 \cdot (I^\uparrow + I^\downarrow) \cdot (1 \pm P)$. The spin polarization is closely related to the spontaneous magnetization $M(T)$, and becomes zero at $T = T_c$ for any binding energy. The quantitative dependence between $P(T)$ and $M(T)/M(0)$ is not a priori clear, since it might depend on the details of the electronic structure at finite temperatures. If no energy shift of the electronic states occur and the decrease in magnetization is purely due to disordering of constant magnetic moments, the relative spin polarization is $P(T)/P(0) = M(T)/M(0)$ at any constant binding energy. This follows from

the above mentioned spin transfomation properties.[20] If the local electronic structure changes also, a more difficult expression is expected,[21]

$$P(T,E) = P_L(T,E) \times M(T)/M(0) \quad . \tag{2}$$

$P_L(E,T)$ is the spin polarization with respect to the direction of the hypothetical local magnetization. In this case, $P(T)/P(0)$, taken at constant binding energy, does not follow the decrease of the relative spontaneous magnetization $M(T)/M(0)$. When P_L(T,E) is independent on temperature, $I^{\uparrow,\downarrow} = I_0(1 \pm M(T)/M(0))$, and the intensity changes are symmetrically around I_0. Otherwise, the intensity changes might be asymmetrically.

4. Experimental Results and Discussion

4.1 Band Dispersions

The interpretation of photoemission spectra is easiest for normal emission since, in this case, the component of the photoelectron wave vector $\vec{k}$ parallel to the surface (k_p) is zero, and only the component $k_\perp$ perpendicular to the surface is a variable.[22] In the present experiment, the photoelectron acceptance cone is centered around the normal direction, and, therefore, the interpretation of the data might first be sought in terms of normal emission. The finite angular acceptance has the effect of additional photocurrent with $k_p(\ )0$. For structures in the spectra which cannot be explained within normal emission, off-normal contributions therefore might be considered.

Dipole selection rules indicate that only Δ_5 symmetry bands along the Γ-H direction (see Fig. 2[23]) are allowed as initial states for the Fe(100)-surface with s-polarized light and normal emission. The band dispersions, as the minority–spin peak position shifts towards the Fermi energy E_F and, once it has reached E_F, the strong drop in intensity has been followed by tuning the photon energy from 70 to 20 eV (see Figs. 3-11). The spin-summed EDCs (Figs. 3a-11a) generally display two peaks, one located near the Fermi energy E_F, and another one at about 2.6 eV binding energy. Besides changes in the relative peak heights and

background, there is not much change with photon energy in the spin-summed EDC's. This observation had been made earlier,[24,25] and from an apparent lack of peak dispersion, it was concluded that a (symmetry-projected) density-of-states is observed.

However, the SREDCs (Figs. 3b-11b) show that actually dispersions take place. The minority-spin intensity drops strongly between 35 and 33 eV, indicating that the minority initial state crosses the Fermi energy. Simultaneously, a majority-spin peak grows near E_F, thereby retaining the peak near E_F in the spin-averaged EDC. Above 35 eV, the minority spin initial state is presumably located in the left half of the Brillouin zone.[26] Below 35 eV, the minority-spin transition apparently takes place from states where the minority-spin band crosses E_F as concluded from the minor influence on photon energy between 31 and 20 eV. The $\downarrow$-spin phototransition between $h\nu = 31$ and 20 eV probably occurs primarily via indirect transition at k-vectors where the $\Delta_5^{\downarrow}$-band crosses E_F. There might also be contributions from states near Γ (corresponding to the $\uparrow$-spin peak around $E_B = 2.6$ eV, which is present at any photon energy). The dominating peak in the majority-spin EDCs for photon energies between 31 and 20 eV is interpreted as due to direct transitions from initial states in the right half of the Brillouin zone. At $h\nu = 31$ eV, the $\uparrow$-spin transition takes place at about 0.7 of the Γ-H separation, as inferred by comparing the peak position near E_F in the $\uparrow$-SREDC with the band structure (Fig. 2). At $h\nu = 21$ eV, the $\uparrow$-transition occurs closer to H. We note that the direct transitions from the $\Delta_5^{\uparrow}$-band dominate the SREDCs between $h\nu = 31$ and 20 eV. A not fully resolved structure at E_F appears additionally in many of the $\uparrow$ - SREDCs in figs. 3b - 11b and is interpreted (26) in terms of a majority-spin surface resonance.

Spin resolved energy distribution curves at $h\nu = 60$ eV are shown in Fig. 12 for two different temperatures. The data at $T/T_c = 0.3$ display the features as reported,[27] but much better resolved. The minority SREDC displays only one single sharp peak (we label $\Gamma_{25}^{\prime\downarrow}$) 0.4 ± 0.2 eV below E_F. In the majority SREDC two peaks are resolved, one located at a binding energy E_B of 2.6 ± 0.2 eV and the other one at 1.2 ± 0.2 eV. The peaks at 2.6 eV and 0.4 eV binding energy

are due to emission from the exchange split Δ_5 symmetry bands near the center of the Brillouin Zone ($\Gamma_{25}^{\prime\uparrow}$ and $\Gamma_{25}^{\prime\downarrow}$). The peak at 1.2 eV is due to emission from the $\Delta_1^{\uparrow}$ band near Γ, which actually is forbidden for strictly normal emission.

4.2 Changes in the SREDCs with Temperature

Upon heating to $T/T_c = 0.85$ the following changes are observed (see Fig. 12): In the minority SREDC, the peak $\Gamma_{25}^{\prime\downarrow}$ diminishes strongly in intensity while its energy-width increases by about a factor of 3, and its peak position shifts by 0.2 eV to larger binding energy. At $E_B = 2.6$ eV, a new broad peak emerges upon heating.

In the majority SREDC, the $\Gamma_{25}^{\prime\uparrow}$ peak at $E_B = 2.6$ eV loses intensity, but much less than its exchange split counterpart. Its position remains nearly unchanged. At the peak position of the minority SREDC ($\Gamma_{25}^{\prime\downarrow}$), a small majority spin intensity gain is observed. We note that the new peak in the $\downarrow$-SREDC around $E_B = 2.6$ eV seems to be broader than the peak due to $\Gamma_{25}^{\prime\uparrow}$ in the $\uparrow$-SREDC.

A marked feature of Fig. 12 is that the binding energy where the up- and down-spin EDCs cross each other is the same for $T/T_c = 0.3$ and $T/T_c = 0.85$ (and also at intermediate temperatures). In other words, the binding energy E_0 where the spin polarization is zero does not change with temperature, and the total intensity also remains constant at that particular energy. At E_0 no transfer of one spin state into the other occurs upon heating (or, the transfers compensate each other in each spin state). This is a different behaviour than around $E_B = 2.6$ eV ($\Gamma_{25}^{\prime\uparrow}$), where only the spin-summed intensity remains (nearly) unchanged. We note also that E_0 is not at the center energy between the exchange split peaks $\Gamma_{25}^{\prime\uparrow}$ and $\Gamma_{25}^{\prime\downarrow}$ due to the presence of emission from $\Gamma_{12}^{\uparrow}$.

Spin-summed EDCs (Fig. 13) show more clearly than Fig. 12 that around the $\Gamma_{25}^{\prime\uparrow}$ peak position only a minor intensity decrease occurs between $T/T_c = 0.3$ and $T/T_c = 0.85$, indicating that losses in the majority SREDC are nearly completely compensated for by the new growing peak in the minority SREDC. (Part of the compensation might also be due to an increased $\downarrow$-spin background.)

This is not the case at the position of the $\Gamma_{25}'^{\downarrow}$ peak, where the total intensity drops down upon heating because of the stronger losses of minority spins as compared to the gains of majority spins. The decrease in intensity at $\Gamma_{25}'^{\downarrow}$ is also larger than expected from the Fermi-Dirac function.

An EDC taken at $T = T_c$ is compared with one taken at room temperature in Fig. 14. During heating to this high temperature, S segregation to the surface occurs quickly and the surface certainly is no longer clean. However, upon cooling down, the peak positions are the same as in the original EDC at $T/T_c = 0.3$, and we observe also again an intensity gain near E_F. Primarily to find the peak position of $\Gamma_{25}'^{\uparrow}$ which is superimposed on a large background, we fitted the EDC at $T = T_c$ with Lorentzian curves. A good fit is obtained with two Lorentzians and a background contribution as the integral over the Lorentzians (normalized appropriately). The fit gives the peak position of $\Gamma_{25}'^{\uparrow}$ as $2.6^{-0.5}_{+0.1}$ eV at $T = T_c$. Fits of this kind are never unique, but the most natural conclusion would be that $\Gamma_{25}'^{\uparrow}$ remains stationary up to T_c. The fit around the $\Gamma_{12}^{\uparrow}$ position with only one Lorentzian is more questionable. It is expected that an even better fit could be obtained with two closely separated Lorentzians. From the decrease in amplitude of $\Gamma_{25}'^{\downarrow}$ up to $T/T_c = 0.85$ it might be concluded that $\Gamma_{25}'^{\downarrow}$ will become very broad and small in amplitude at higher temperatures. Therefore, the broad peak at $E_B = 0.8$ eV probably is mostly due to an unshifted $\Gamma_{12}^{\uparrow}$ and also due to a remainder of $\Gamma_{25}'^{\downarrow}$.

The balancing of gains and losses in intensity observed at the position of $\Gamma_{25}'^{\uparrow}$ could be interpreted in terms of fluctuations of a constant magnetic moment around the spontaneous magnetization axis resulting in a mixing of spins in the spin analyzer (even of internally pure spin states with respect to the instantaneous direction of the local moment). However, the different behavior at the position of $\Gamma_{25}'^{\downarrow}$ indicates already that this model is not completely adequate.

For 35 eV, spin-summed EDCs taken at different temperatures are shown in Fig. 15. Compared to the 60 eV data, the intensity changes are small.

In Fig. 16, SREDCs taken at different temperatures for $h\nu = 31$ are shown,

and in Fig. 17 for hν = 21 eV. There is a marked difference to the hν = 60 eV data (Figs. 12 and 13): Instead of a decrease in spin-summed intensity near E_F we observe a strong increase in total photocurrent upon heating for photon energies of 31 and 21 eV. The SREDCs demonstrate that it is a doubling of minority-spin intensity and a comparatively small decrease in majority-spin intensity causing the gain in total intensity. This asymmetry excludes an interpretation of the majority- and minority-spin intensity changes as transverse fluctuations of a local magnetic moment. We conclude that the reason for the minority spin intensity increase upon heating is a build-up of minority-spin density of states at and slightly below E_F near k-vectors where the $\uparrow$-spin phototransition occurs efficiently ($\sim$ 0.7 of the Γ-H separation at 31 eV). This would allow for direct transitions for $\downarrow$-electrons from these temperature-induced initial states with the result of an increase in $\downarrow$-photocurrent. The majority-spin phototransition does not suffer from the Fermi energy cut-off, explaining its less pronounced temperature dependence. However, its intensity decreases, which could be explained by an upwards shift of the majority-spin band.

The different character of the spin-rearrangement upon heating is seen again in Fig. 18, where the spin resolved intensities taken at a constant binding energy are shown for two cases, hν = 60 eV, E_B = 2.6 eV, and hν = 30 eV, E_B = 0.8 eV. The balancing of spins for the first case is in agreement with above mentioned findings on the behavior of $\Gamma_{25}^{\prime\uparrow}$ and the increase in $\downarrow$-intensity is in accordance with the data in Fig. 16. The 30 eV data do not much differ from the 31 eV data discussed above.

4.3 Changes in Angular Width with Temperature

A reason for the strong intensity loss upon heating at the position of $\Gamma_{25}^{\prime\downarrow}$ is the increase in angular width of the minority-spin photoemission cone which is sharply peaked to the normal direction at low temperature. This is seen in Fig. 19, where the beam profiles obtained by sweeping the beam across the entrance aperture of the electron energy analyzer are compared for two different temperatures. The electron spectrometer was set to fixed binding energy (equal to the Fermi energy in this case). The larger width ΔU in deflection voltage

reflects a broader image of the emitting area on the aperature over which the beam is swept. The increase in width ΔU is due to geometrical aberrations of the electron lens systems, and $\Delta U = C \cdot \Delta\alpha^3$.[28] The constant C is presently being calculated from the computed trajectories.

Only a very small increase in angular width with temperature is observed at the position of the majority-spin peak ($\Gamma_{25}^{\prime\uparrow}$) upon heating in agreement with the stated nearly-constant spin-summed intensity.

Since the photoelectron emission angle is determined by the internal k-vector, the broadening is interpreted as a $\vec{k}$-broadening of the initial state. The $\vec{k}$-broadening due to disordering of the local magnetic moments is connected to the energy broadening by the relation $\Delta k = \Delta E \cdot \frac{\partial k}{\partial E}$.[29] Since $\Gamma_{25}^{\prime\downarrow}$ is broadened in energy much more than $\Gamma_{25}^{\prime\uparrow}$, the much stronger $\vec{k}$-broadening of $\Gamma_{25}^{\prime\downarrow}$ then $\Gamma_{25}^{\prime\uparrow}$ can be understood.

4.4 Surface Magnetism

We have plotted in Fig. 20 the relative spin polarization P(T) corresponding to the data in Fig. 18 as function of temperature, normalized to an extrapolated P(0) = 1. Also indicated in the figure are calculations of the layer-dependent magnetization as function of temperature. The calculations were performed in the mean-field approximation with equal inter- and intra-layer coupling constants similarily as by Wolfram et al.[29] It is seen that P(T) behaves much like the first to second layer magnetization temperature dependence. For hv = 30 eV (Fig. 20b), it is actually closely to the first layer magnetization. This behavior, however, might be incidental and could be an indication of the validity of Eq. (2), since the changes in polarization are due to the strong minority-current increase, which has been interpreted above as an effect due to the build-up of $\downarrow$-spin states around k = 0.7 of the Γ-H separation.

4.5 Comparison with the Disordered - Local - Moment Theory

We have seen in the last paragraph that the data most probably represent the magnetic properties of just a few (1 - 3) surface crystal planes. However, the room temperature data can be interpreted based primarily on the bulk electronic

structure, indicating that intrinsic surface-effects are small. We might therefore expect that also the finite temperatures properties can be interpreted at least qualitatively from predictions for the bulk.

The only present theory which makes quantitative predictions on the changes in electronic structure with temperature, is the disordered - local - moment theory.[5,31] Within this theory, the electronic structure of Fe above T_c has been calculated from first principles in the KKR-CPA approximation, treating ferromagnetism at finite temperature as a binary alloy problem, and the right Curie temperature has been obtained, for example.[29] Within this theory, also the so-called Bloch spectral function $A_b(k,E)$ has been calculated,[5,31] a quantity which can be interpreted as the density of states per k-point. I.e., at $T = 0$, $A_b(k,E)$ is a delta function at the Bloch energy eigenvalues. At finite temperatures, $A_b(k,E)$ generally becomes smeared out in k and E as a result of disorder. One of the predictions that have been made was that $\Gamma_{25}'^{\uparrow}$ is nearly stationary in energy (a shift of about 0.7 eV has been predicted[5,29] as compared to the exchange splitting at Γ of 2.2 eV), whereas at H, the exchange splitting should vanish above T_c. The decrease in the exchange splitting leads to a large amplitude of the Bloch spectral function at E_F around 0.7 of the Γ-H separation above T_c.[31] At $T = 0$, it would have a large amplitude only where the $\Delta_5^{\uparrow,\downarrow}$ bands cross E_F, i.e. at 0.9 and 0.5 of the Γ-H separation, respectively (see fig. 2). This build-up of density of states would appear gradually (proportional to the decrease of the spontaneous magnetization) with temperature. Furthermore, a strong broadening of $\Gamma_{25}'^{\downarrow}$ in both k and energy with temperature has been predicted, $\Gamma_{25}'^{\downarrow}$ becoming completely washed-out.[29]

By comparing with the experimental data which have been discussed above, we conclude that these predictions are qualitatively fulfilled. This is most obvious for the data taken near Γ ($h\nu = 60$ eV), although the shift of $\Gamma_{25}'^{\uparrow}$ experimentally seems to be smaller than predicted. We also observed the strong broadening of $\Gamma_{25}'^{\downarrow}$ in energy and angle ($\vec{k}$). The predicted build-up of the Bloch spectral function around 0.7 Γ-H at and below E_F is seen most eluciadely in the increase of minority-spin photocurrent in the data taken at $h\nu = 31$ and 21 eV, Figs.

16 and 17. The phototransition would like to occur as effective for minority-spin electrons than for majority-ones, but at room temperature, the minority band for k-vector in the right half of the Brillouin zone, where the majority-spin phototransition takes place, is located above E_F. The strong increase in minority-spin photocurrent upon heating is therefore interpreted as a build-up of minority-spin initial density of states upon heating in agreement with the calculations in the disordered-local-moment picture.

5. Conclusion

The new data might serve as a test for quantitative calculations. A finite temperature theory of ferromagnetism (and of the photoemission process) has to explain simultaneously the nearly stationary character of $\Gamma_{25}^{\prime\uparrow}$, the $\vec{k}$-broadening of $\Gamma_{25}^{\prime\downarrow}$, and, the apparent shift of the $\Delta_5^{\downarrow}$ band for large k-vectors. Recent self-consistent calculations by Gyorffy et al [5,31] based on the 'disordered-local-moment picture of Fe are in qualitative agreement with these findings. The data demonstrates also that the photoelectron energy distribution might become deformed at high temperatures due to binding-energy dependent losses of photoemission intensity.

Acknowledgements

We would like to acknowledge fruitful and stimulating discussion with J. Callaway, D.M. Edwards, B.L. Gyorffy, R. Feder, M.B. Stearns and G.M. Stocks, and to thank Ing. D. Hoffmann for his excellent technical support. We gratefully acknowledge the technical support of the BESSY staff. One of us (E.K.) wishes to thank E.L. Garwin for the hospitality at SLAC during paper preparation.

References

1. D.E. Eastman, J.F. Janak, A.R. Williams, R.V. Coleman, and G. Wendin, J. Appl. Phys. 50, 7423 (1979).
2. H. Capellmann, J. Phys, F4, 1466 (1974).
3. V. Korenmann, J.L. Murray, and R.E. Prange, Phys. Rev. B16, 4032 (1977).
4. M.V. You, V. Heine, A.J. Holden, P.J. Lin-Chung, Phys. Rev. Lett. 44, 1282 (1980).
5. B.L. Gyorffy, J. Kollar, A.J. Pindor, J. Staunton, G.M. Stocks, and H. Winter, Proceedings of the 3d-Metallic Magnetism Workshop, 832I18T, Grenoble (1983), p. 121.
6. H. Hasegawa, J. Phys. Soc. Jap. 49, 963 (1980).
7. J.W. Lynn, Phys. Rev B11, 2624 (1975).
8. O. Steinsvoll, C.F. Majkrzak, G. Shirane, and J. Wicksted, Phys. Rev. Lett. 51, 300 (1983).
9. A. J. Holden, V. Heine, and J. H. Samson, J. Phys. F14, 1005 (1984).
10. D. E. Eastman, F. J. Himpsel, and J. A. Knapp, Phys. Rev. Lett. 44, 95 (1978).
11. A.M. Turner and J.L. Erskine, Phys. Rev. B25, 1983 (1982).
12. Part of this work will be published in Phys. Rev. Lett.
13. H. Capellmann, J. Magn. Magn. Mat. 28, 250 (1982).
14. A detailed analysis of the width of structures in photoemission EDCs is in preparation.
15. H. Hopster, R. Raue, G. Güntherodt, E. Kisker, R. Clauberg, and M. Campagna, Phys. Rev. Lett. 51, 829 (1983).
16. W. Gudat, E. Kisker, G.M. Rothberg, and C. Depautex, Nucl. Instr. Meth.

195, 233 (1982).

17. E. Kisker, R. Clauberg, and W. Gudat, Rev. Sci. Instr. 53, 1137 (1982).
18. K. Schröder, to be published.
19. G. Broden, G. Gafner, and H.P. Bonzel, Appl. Phys. 13, 333 (1977).
20. See, for example, D. M. Edwards, J. Phys. C L327 (1983), where a similar expression is derived for spin polarized field emission.
21. E. Kisker, J. Chem. Phys. 87, 3597 (1983).
22. See, for example, N. V. Smith in: Topics in Applied Physics, Vol. 28 (Photoemission in Solids I), M. Cardona and L. Ley, ed., Springer (1978).
23. C. S. Wang and J. Callaway, Phys. Rev. B16, 2095 (1977).
24. A. Schultz, R. Courths, H. Schultz, and S. Hüfner, J. Phys. F9, L41 (1979).
25. P. Heimann and N. Neddermeyer, Phys. Rev. B18, 3537 (1978).
26. For a theoretical interpretation in terms of the band structure, see R. Feder, U. Baier, A. Rodriguez, and E. Kisker, to be published.
27. R. Feder, W. Gudat, E. Kisker, K. Schröder, and A. Rodriguez, Sol. State Comm. 46, 619 (1983).
28. See, for example, "Electron Optics," O. Klemperer, Cambridge (1953).
29. G.M. Stocks, private communication.
30. T. Wolfram, R. E. DeWames, W. F. Hall, and P. W. Palmberg, Surf. Sci. 28, 45 (1971).
31. J. Staunton, B. L. Gyorffy, A. J. Pindor, G. M. Stocks, and H. Winter, to be published.

Figure Captions

Figure 1 Schematic of the apparatus for spin-, angle- and energy resolved photoemission with synchrotron radiation.

Figure 2 Band structure of Fe along the Γ-H direction in the Brillouin Zone sampled by the present experiments.[23] The energy scale at the top of the figure indicates the initial state k-vector ($k_\perp$) for the phototransition from the $\Delta_5^\uparrow$ band.

Figure 3 Spin-summed (a) and spin resolved energy distribution curves (b) from Fe(100) for s-polarized light and normal emission at 70 eV photon energy. Δ = majority-spin ($\uparrow$) EDC, ∇ = minority-spin ($\downarrow$) EDC.

Figure 4 Same as Fig. 3, except $h\nu = 60$ eV.

Figure 5 Same as Fig. 4, except $h\nu = 41$ eV.

Figure 6 Same as Fig. 5, except $h\nu = 35$ eV.

Figure 7 Same as Fig. 6, except $h\nu = 33$ eV.

Figure 8 Same as Fig. 7, except $h\nu = 31$ eV.

Figure 9 Same as Fig. 8, except $h\nu = 25$ eV.

Figure 10 Same as Fig. 9, except $h\nu = 21$ eV.

Figure 11 Same as Fig. 10, except $h\nu = 20$ eV.

Figure 12 Spin-resolved energy distribution curves at $h\nu = 60$ eV for two temperatures ($\tau = T/T_c = 0.3$ and $T/T_c = 0.85$).

Figure 13 Spin-summed energy distribution curves from Fe(100) at $h\nu$ = 60 eV, taken at different temperatures.

Figure 14 Spin-summed energy distribution curves taken at T = 0.3 and T = T_c normalized to equal peak heights for hv = 60 eV.

Figure 15 Spin-summed energy distribution curves at $h\nu$ = 35 eV taken at T/T_c = 0.3, 0.65, 0.77.

Figure 16 Spin- and angle-resolved energy-distribution curves of Fe(001) at 31 eV photon energy for T/T_c = 0.3 and 0.85. (unsmoothed data).

Figure 17 Spin- and angle-resolved energy-distribution curves of Fe(001) at 21 eV photon energy for T/T_c = 0.3 and 0.7.

Figure 18 Spin-resolved intensities as function of temperature for $h\nu$ = 60 eV and 2.6 eV binding energy ($\Gamma_{25}^{\prime\uparrow}$) (a) and for $h\nu$ = 30 eV, E_B = 0.8 eV (b).

Figure 19 Beam profile as obtained when sweeping the electron beam across the entrance aperture of the electron spectrometer by ramping the voltage across a set of deflection plates in front of the aperture, at two different sample temperatures (T/T_c = 0.3 and T/T_c = 0.85).

Figure 20 Spin polarization as function of temperature taken at 2.6 eV binding energy ($\Gamma_{25}^{\prime\uparrow}$) at $h\nu$ = 60 eV (a) and, at 0.8 eV binding energy at $h\nu$ = 30 eV (b). The data are normalized to the room temperature spin polarization.

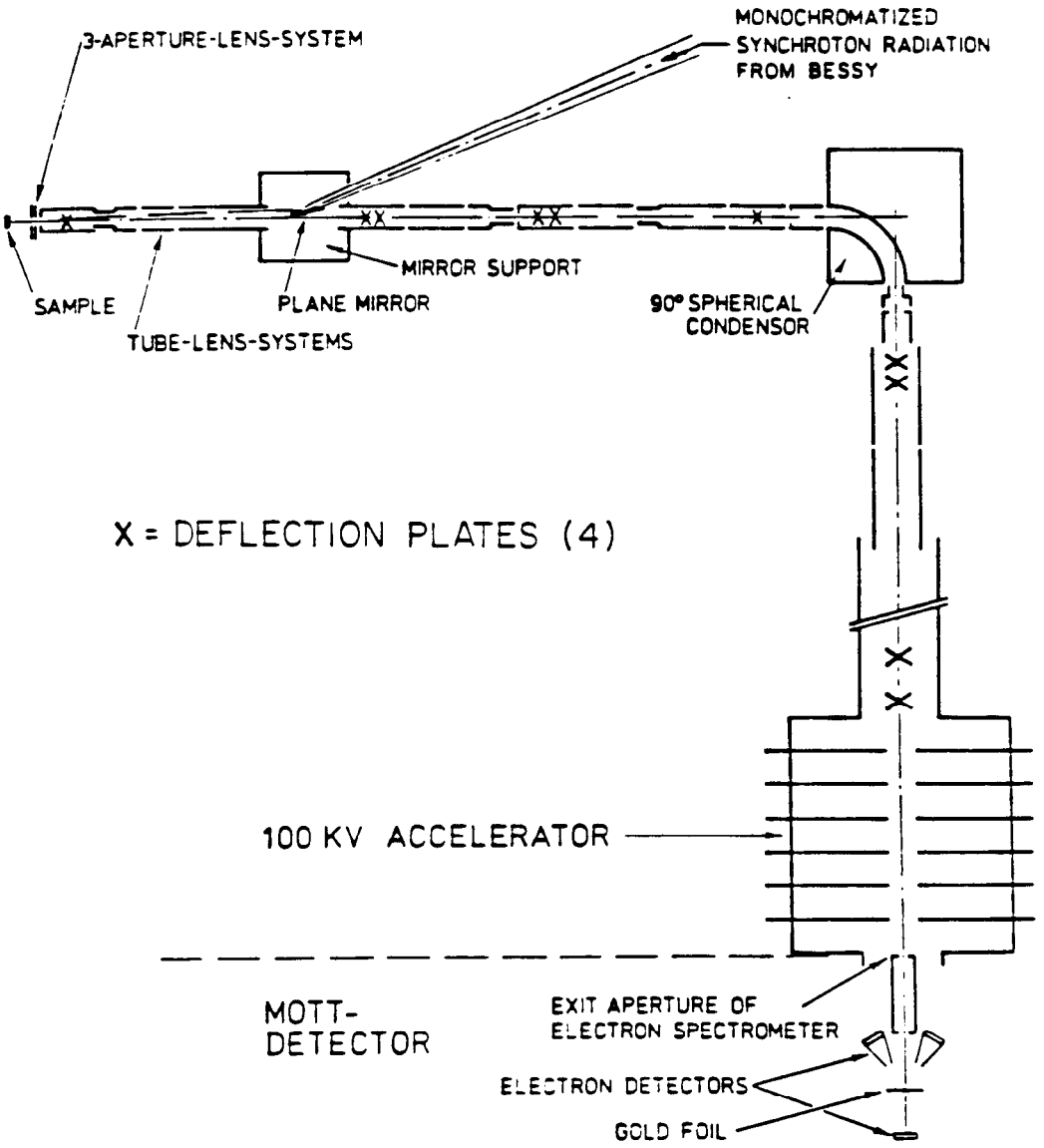
3-APERTURE-LENS-SYSTEM
MONOCHROMATIZED
SYNCHROTON RADIATION
FROM BESSY
MIRROR SUPPORT
SAMPLE
PLANE MIRROR
90° SPHERICAL
CONDENSOR
TUBE-LENS-SYSTEMS
X = DEFLECTION PLATES (4)
100 KV ACCELERATOR
MOTT-
DETECTOR
EXIT APERTURE OF
ELECTRON SPECTROMETER
ELECTRON DETECTORS
GOLD FOIL

Fig. 1

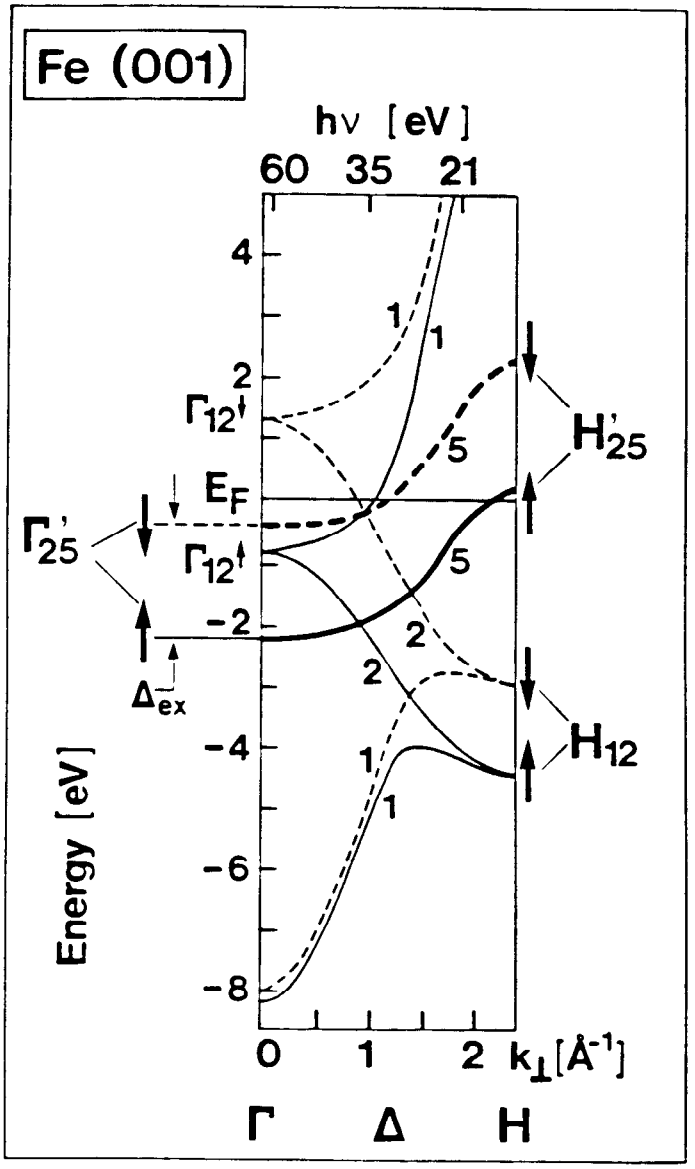
Fe (001)
hν [eV]
60 35 21
4
2
-2
-4
-6
-8
Γ12↑
EF
Γ25'
Γ12↓
Δex
H'25
H12
1
1
5
5
2
2
1
1
Energy [eV]
0 1 2 k⊥[Å-1]
Γ Δ H

Fig. 2

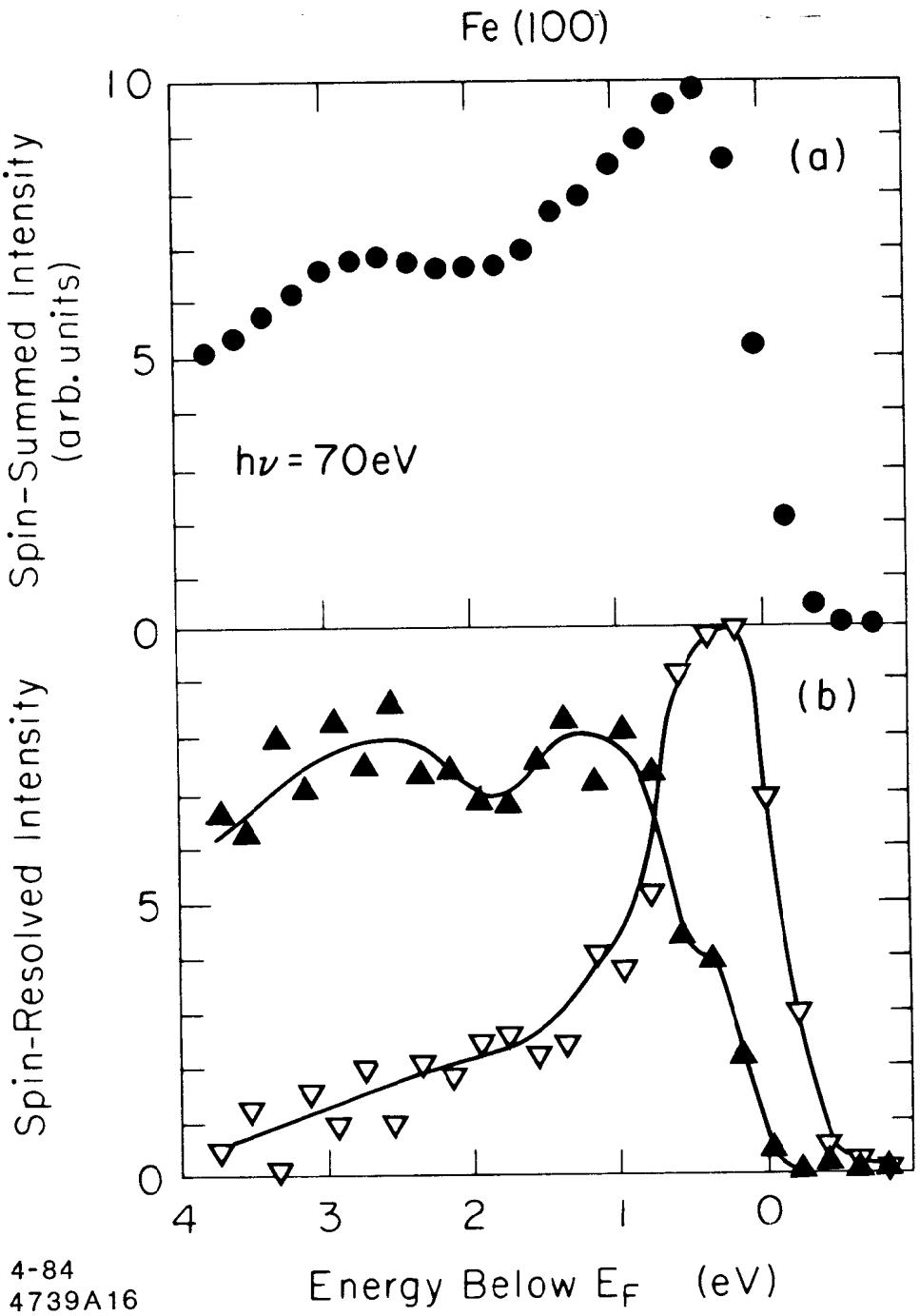
Fe (100)
10
5
0
(a)
hν = 70eV
Spin-Summed Intensity
(arb. units)
Spin-Resolved Intensity
5
0
(b)
4
3
2
1
0
Energy Below E_F (eV)
4-84
4739A16

Fig. 3

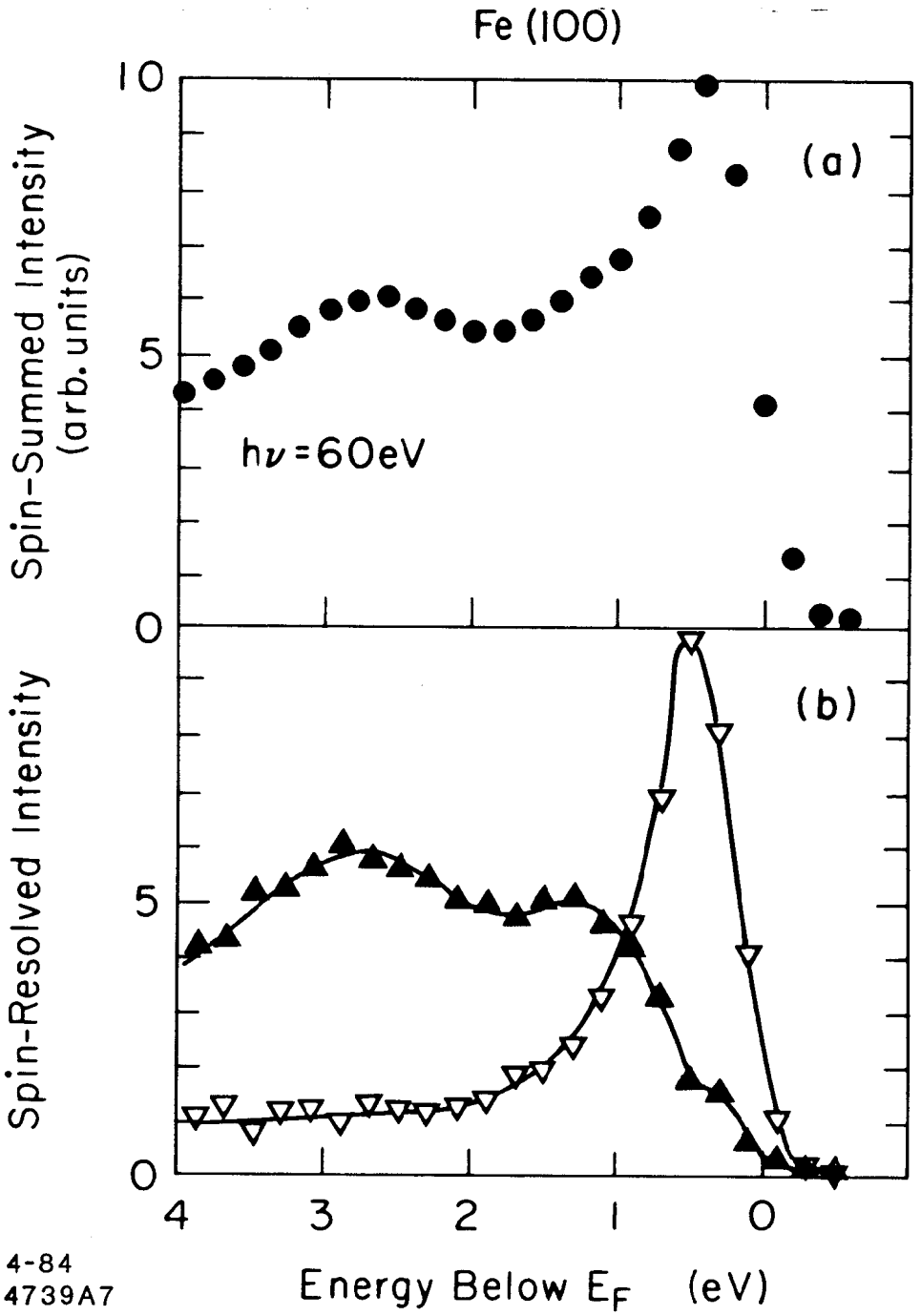
Fe (100)
10
5
0
Spin-Summed Intensity
(arb. units)
(a)
hν = 60eV
(b)
Spin-Resolved Intensity
5
0
4
3
2
1
0
Energy Below E_F (eV)
4-84
4739A7

Fig. 4

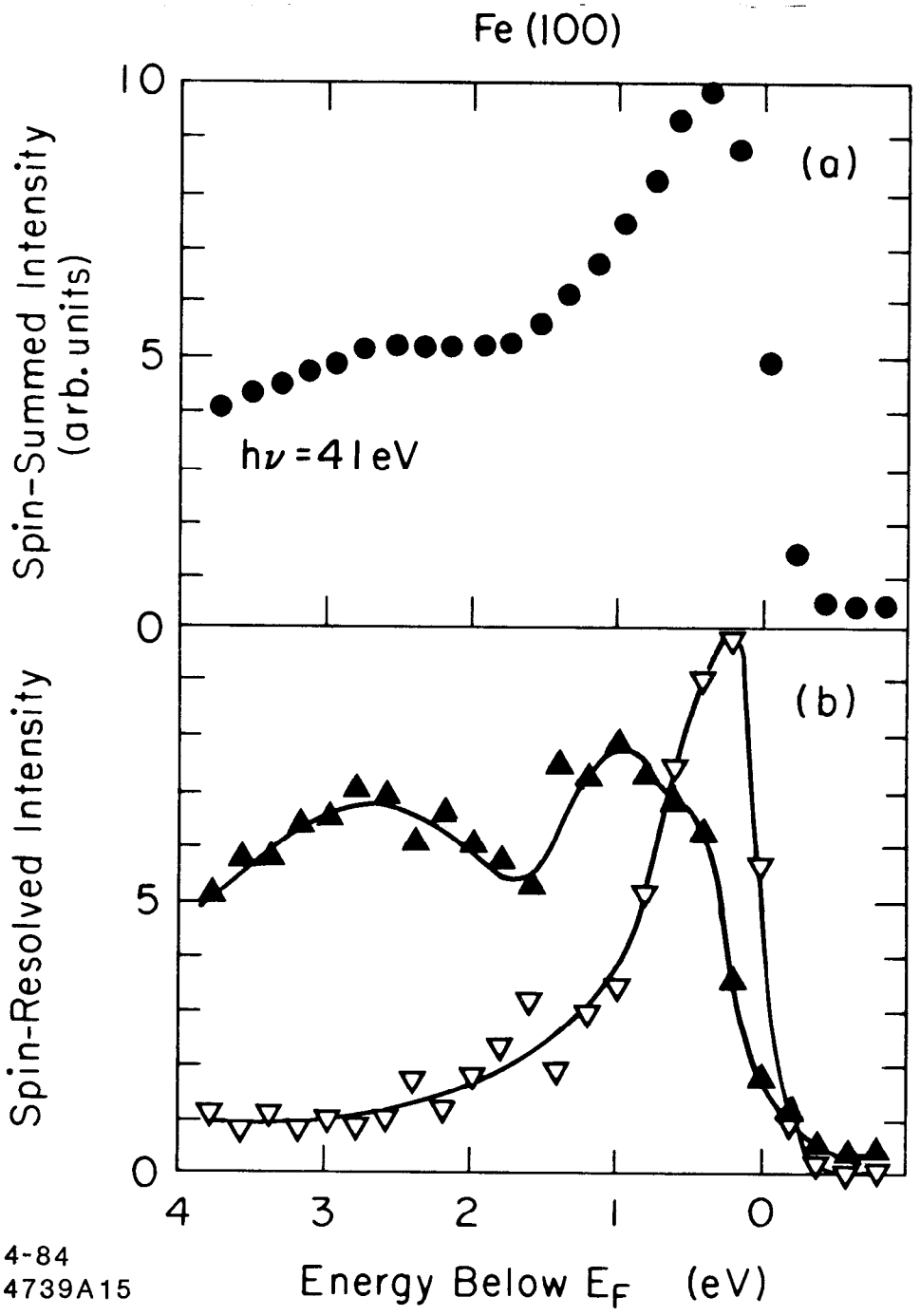
Fe (100)
10
5
0
Spin-Summed Intensity
(arb. units)
(a)
hν = 41 eV
Spin-Resolved Intensity
(b)
5
0
4
3
2
1
0
Energy Below E_F (eV)
4-84
4739A15

Fig. 5

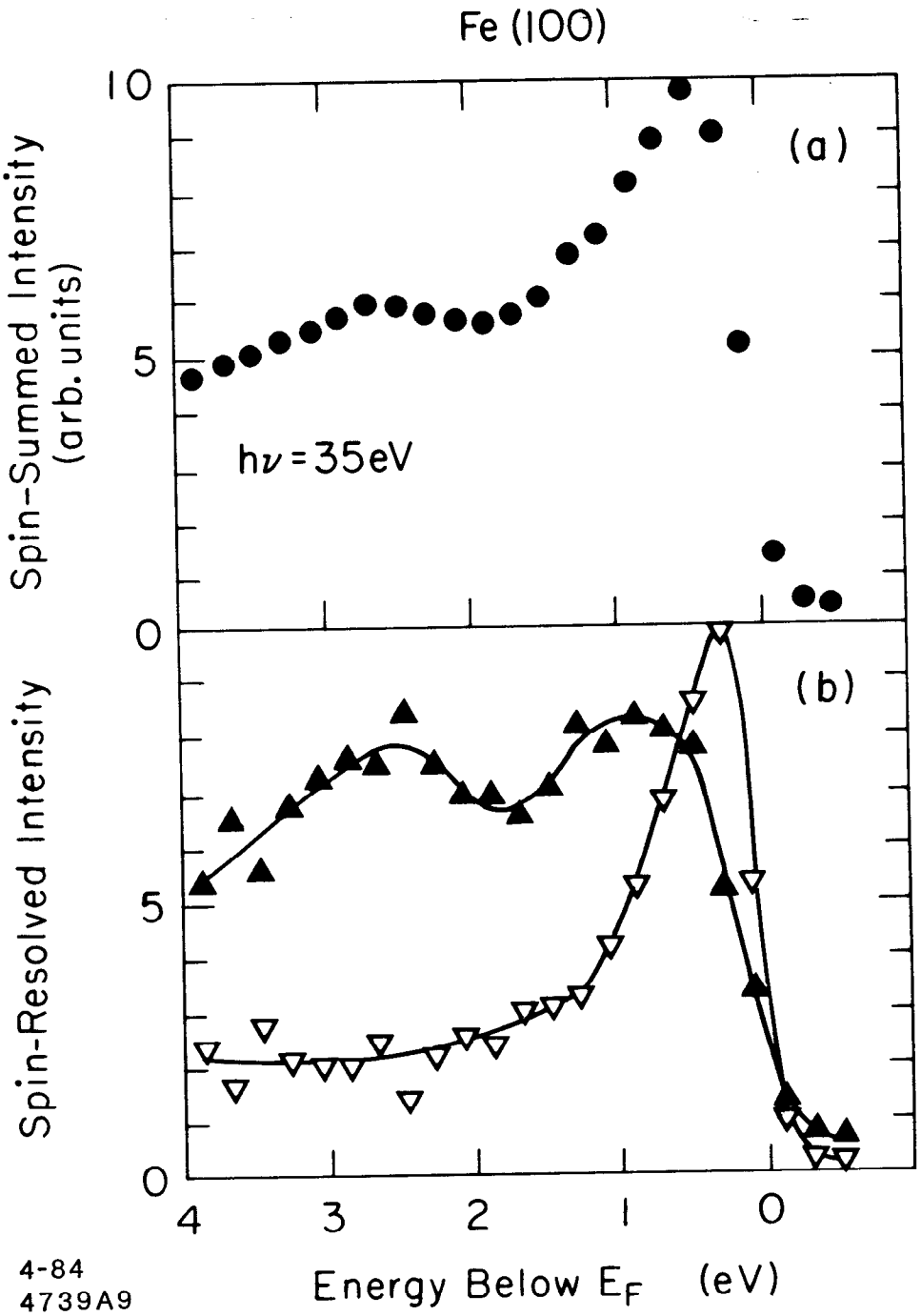
Fe (100)
10
5
0
(a)
Spin-Summed Intensity
(arb. units)
hν = 35eV
(b)
Spin-Resolved Intensity
5
0
4
3
2
1
0
4-84
4739A9
Energy Below E_F (eV)

Fig. 6

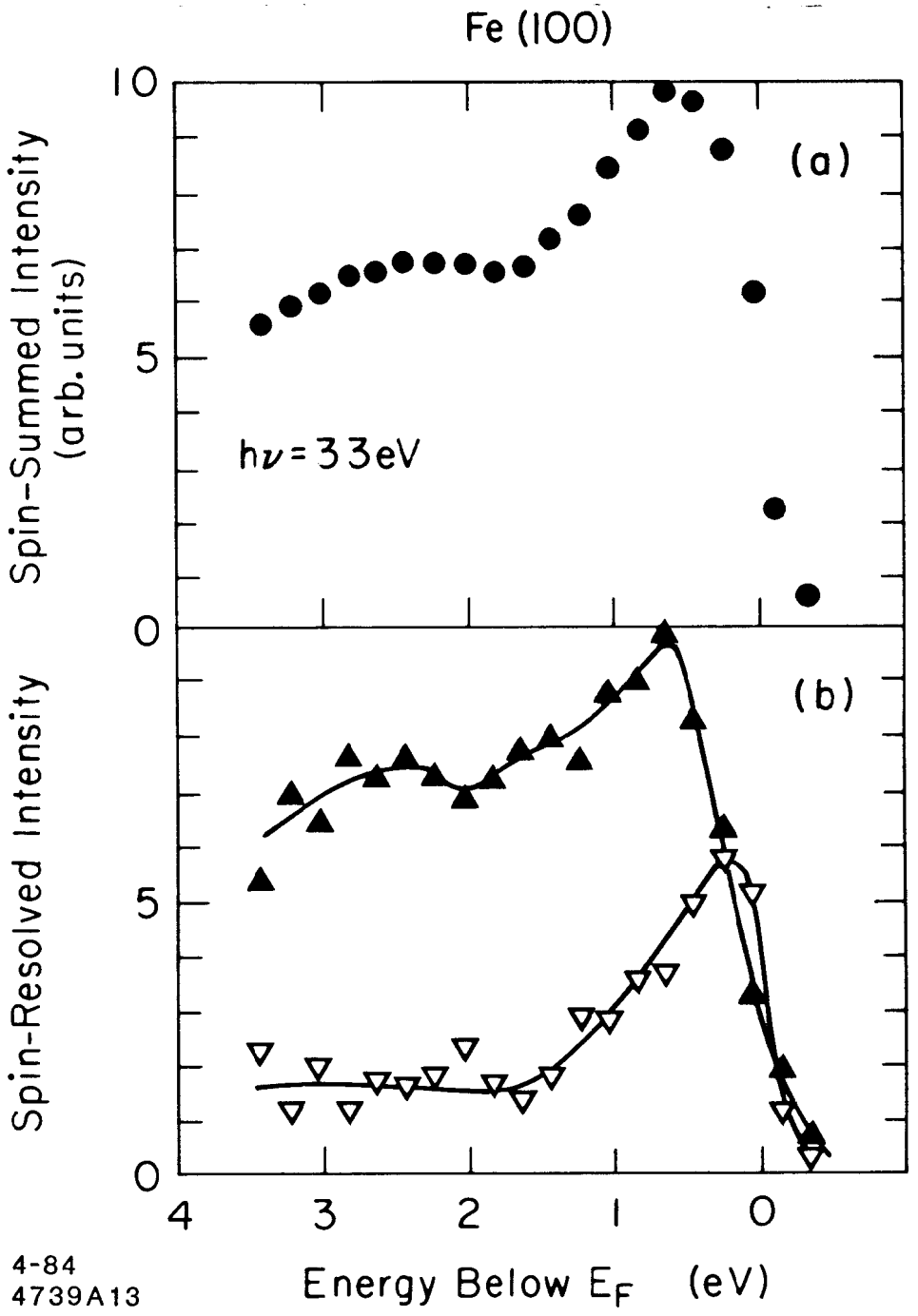
Fe (100)
10
5
0
Spin-Summed Intensity
(arb. units)
(a)
hν = 33eV
Spin-Resolved Intensity
(b)
5
0
4
3
2
1
0
4-84
4739A13
Energy Below E_F (eV)

Fig. 7

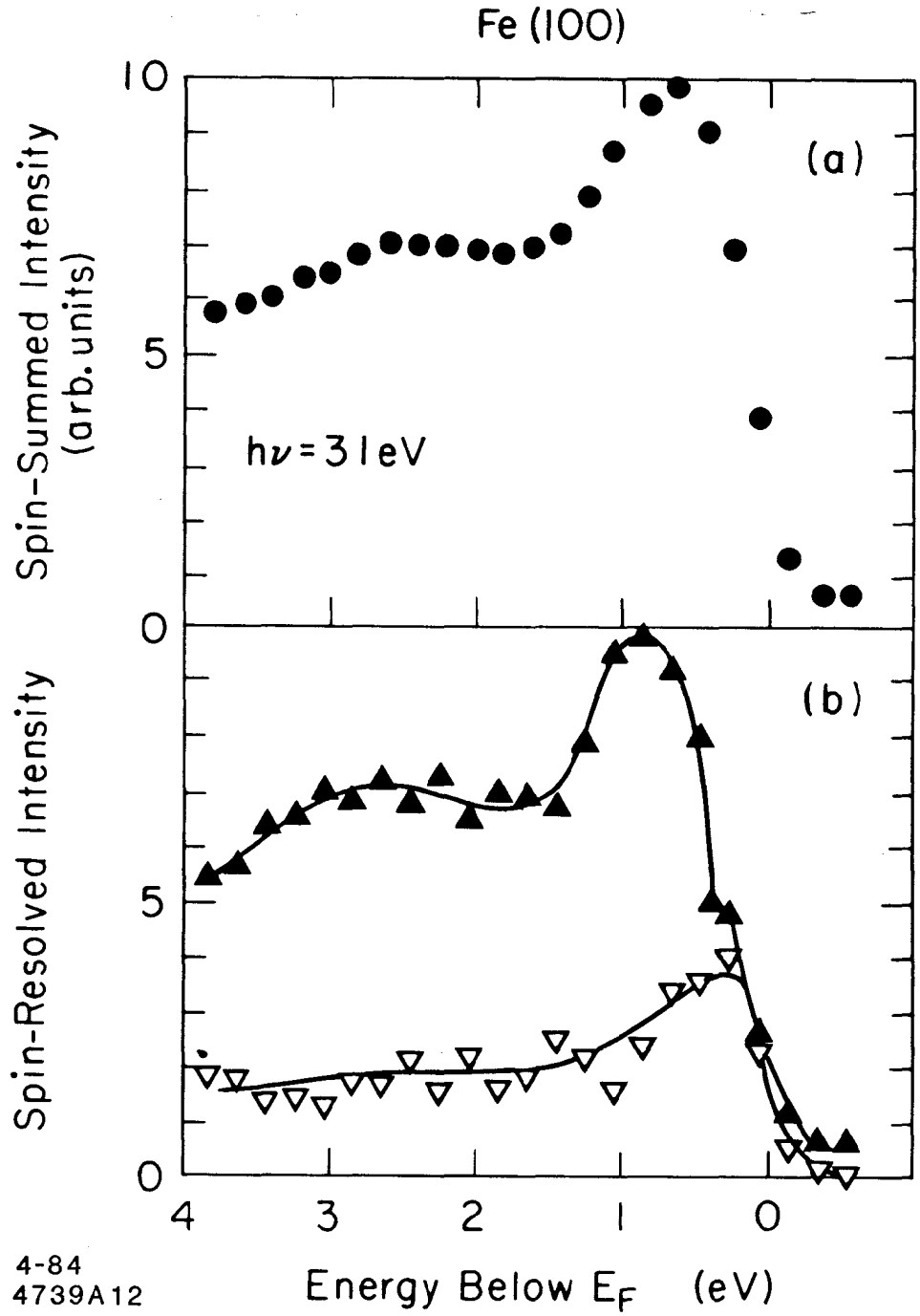
Fe (100)
10
5
0
(a)
Spin-Summed Intensity
(arb. units)
hν = 31 eV
(b)
Spin-Resolved Intensity
5
0
4
3
2
1
0
4-84
4739A12
Energy Below E_F (eV)

Fig. 8

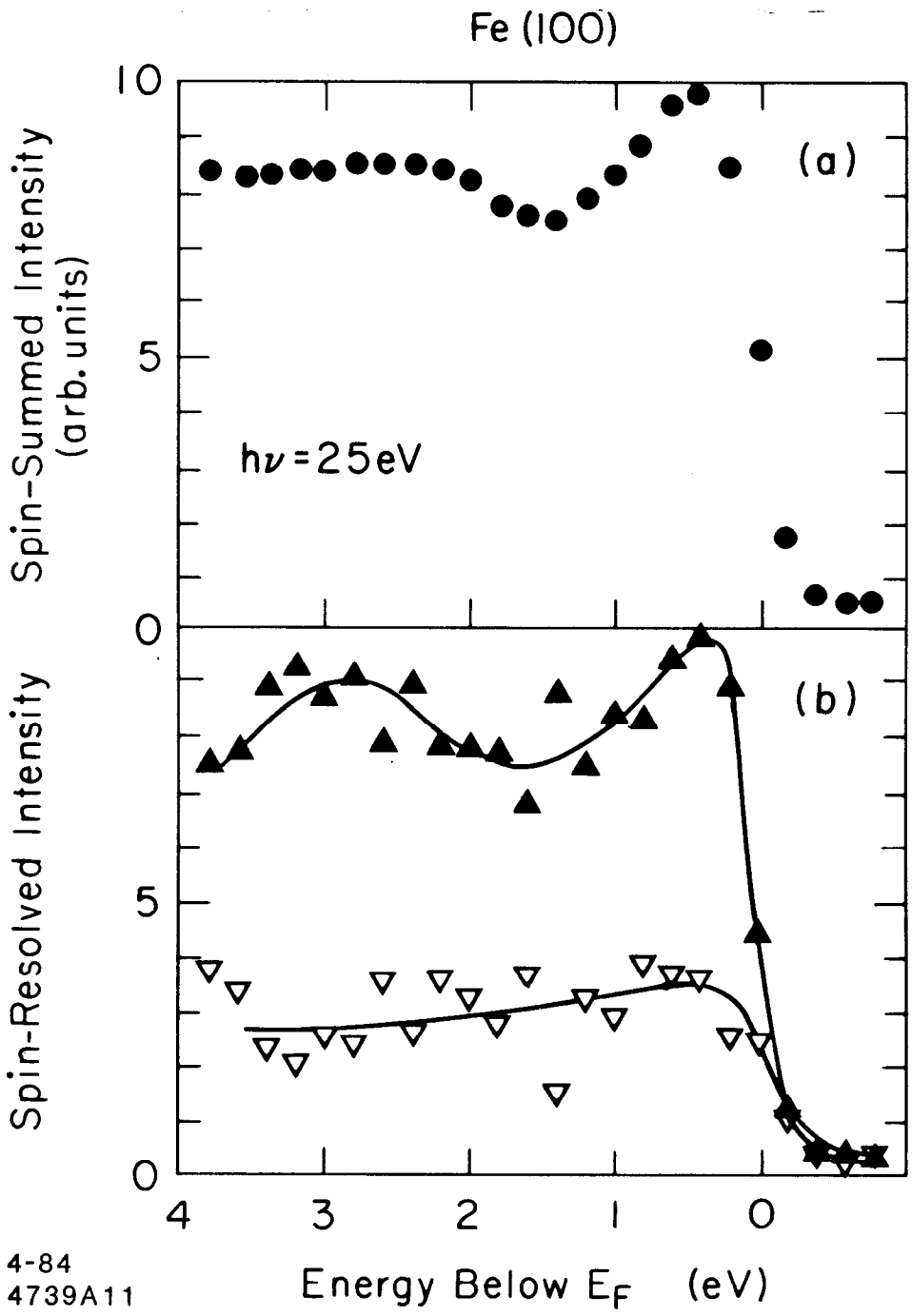
Fe (100)
10
5
0
Spin-Summed Intensity
(arb. units)
(a)
hν = 25eV
Spin-Resolved Intensity
(b)
5
0
4
3
2
1
0
Energy Below E_F (eV)
4-84
4739A11

Fig. 9

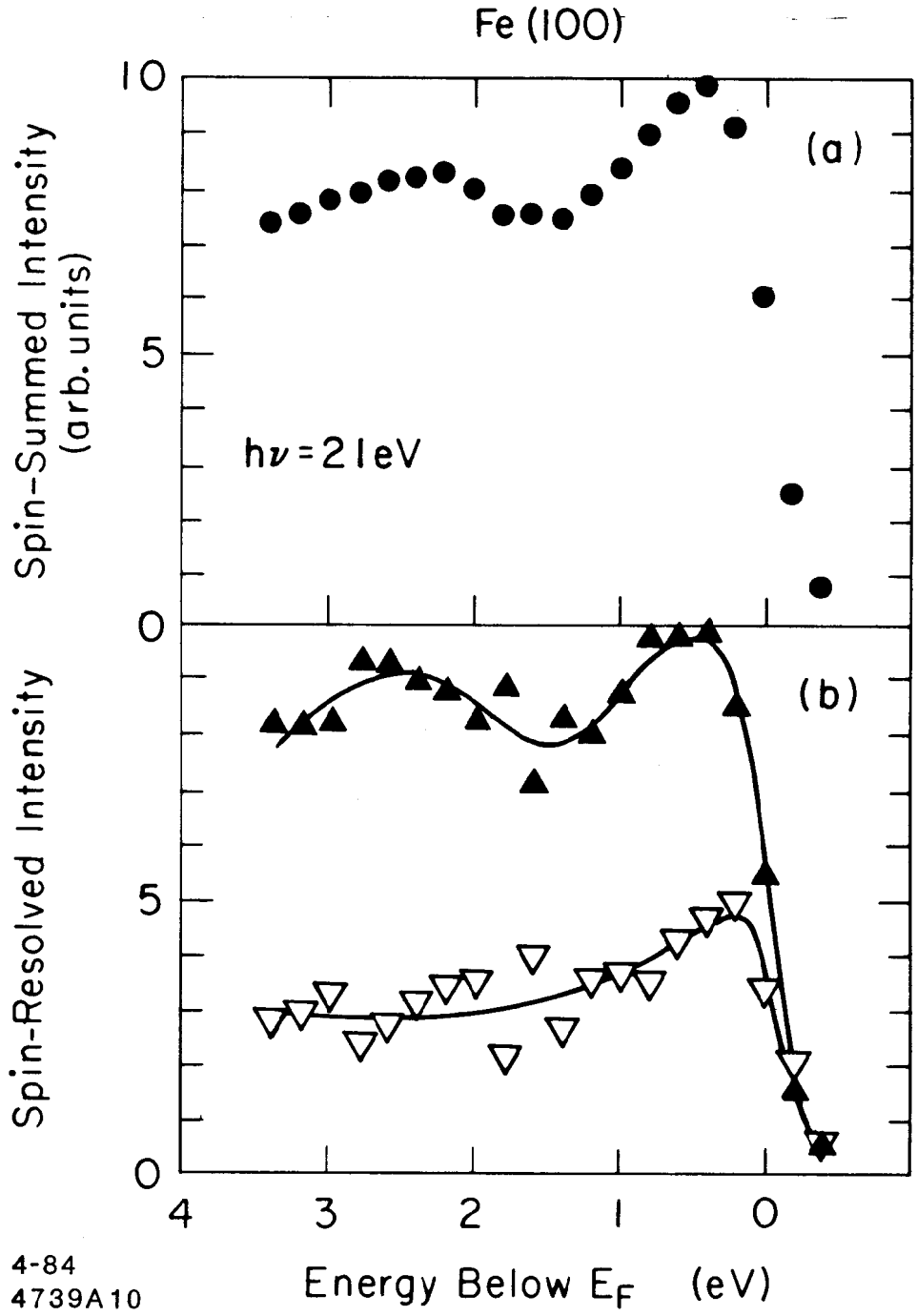
Fe (100)
10
5
0
Spin-Summed Intensity
(arb. units)
(a)
hν = 21eV
Spin-Resolved Intensity
(b)
5
0
4
3
2
1
0
Energy Below E_F (eV)
4-84
4739A10

Fig. 10

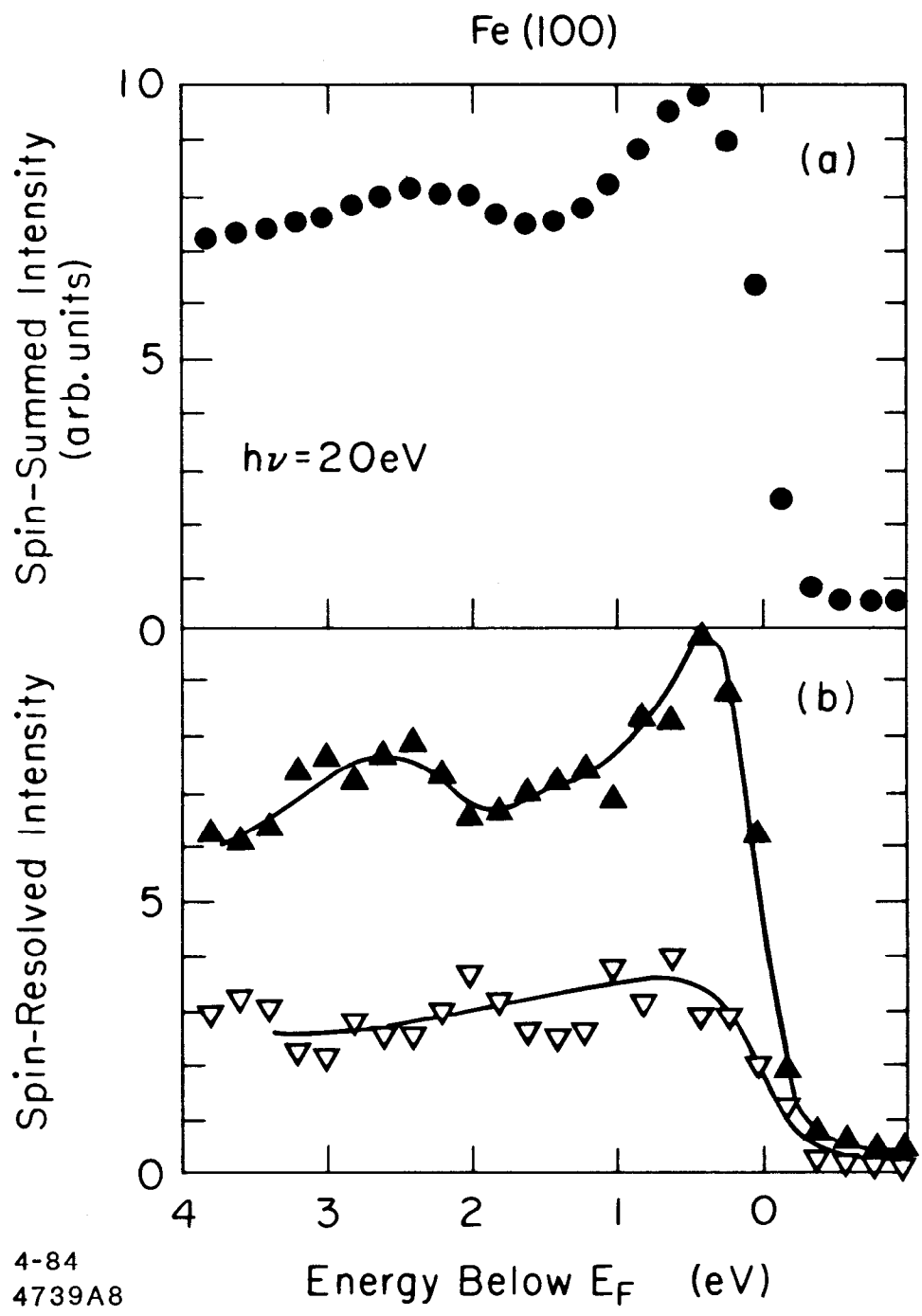
Fe (100)
10
5
0
(a)
Spin-Summed Intensity
(arb. units)
hν=20eV
5
0
(b)
Spin-Resolved Intensity
4
3
2
1
0
Energy Below E_F (eV)
4-84
4739A8

Fig. 11

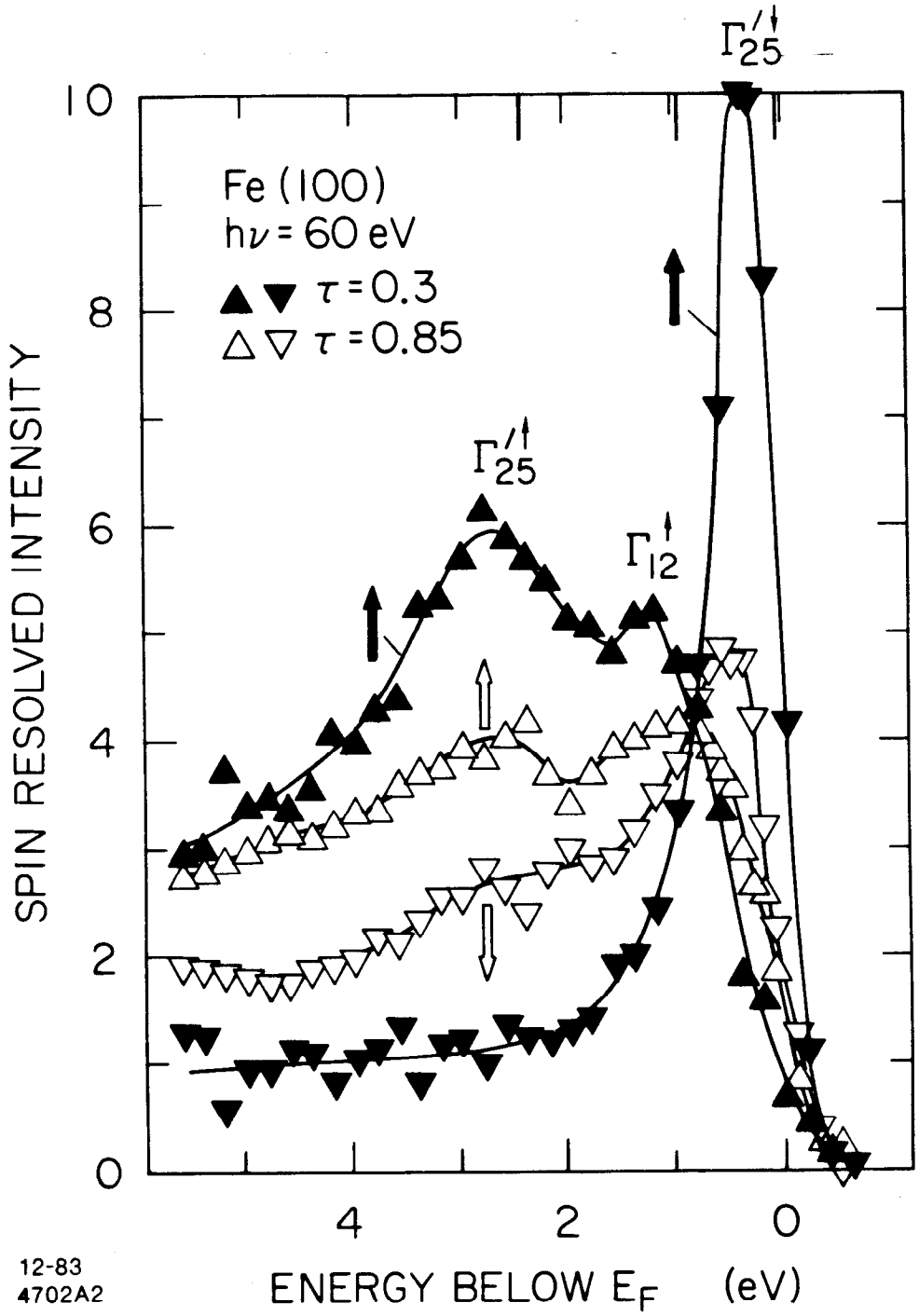
Fe (100)
hν = 60 eV
▲▼ τ = 0.3
△▽ τ = 0.85
Γ'25↑
Γ'25↓
Γ12↑
SPIN RESOLVED INTENSITY
ENERGY BELOW EF (eV)
0
2
4
6
8
10
4
2
0
12-83
4702A2

Fig. 12

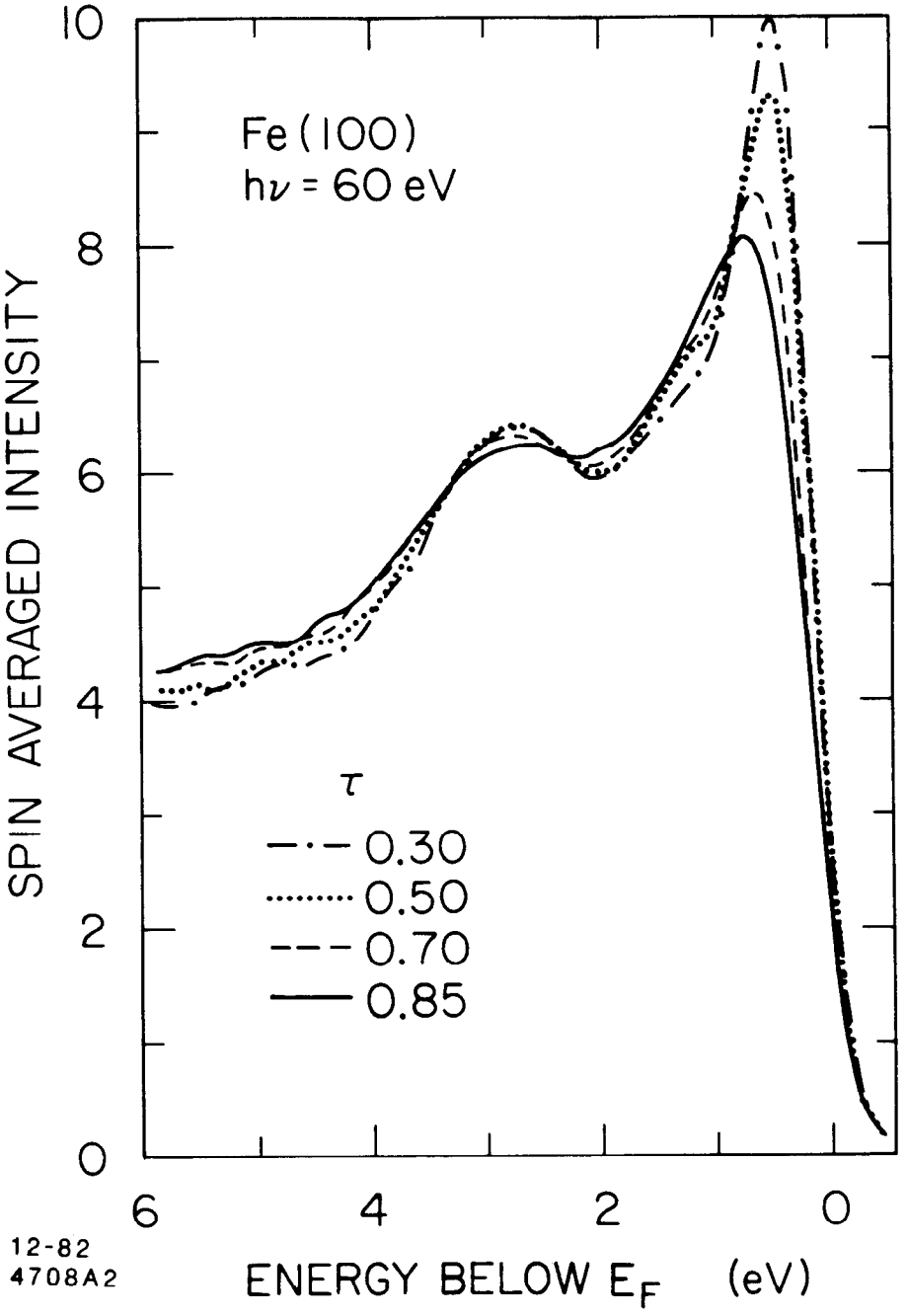
Fe(100)
hν = 60 eV
τ
0.30
0.50
0.70
0.85
SPIN AVERAGED INTENSITY
ENERGY BELOW E_F (eV)
10
8
6
4
2
0
6
4
2
0
12-82
4708A2

Fig. 13

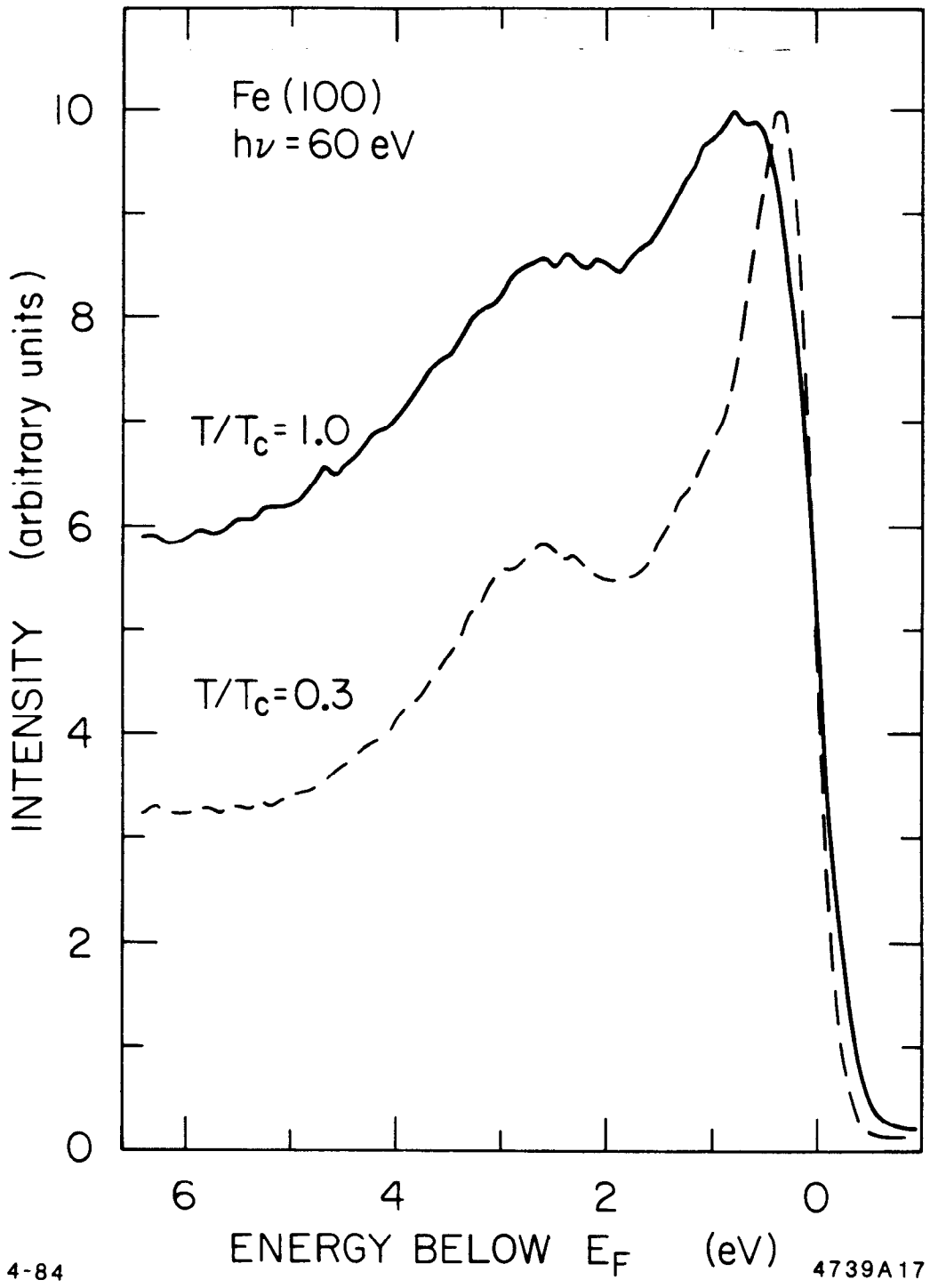
Fe (100)
hν = 60 eV
T/Tc = 1.0
T/Tc = 0.3
INTENSITY (arbitrary units)
0
2
4
6
8
10
6
4
2
0
ENERGY BELOW EF (eV)
4-84
4739A17

Fig. 14

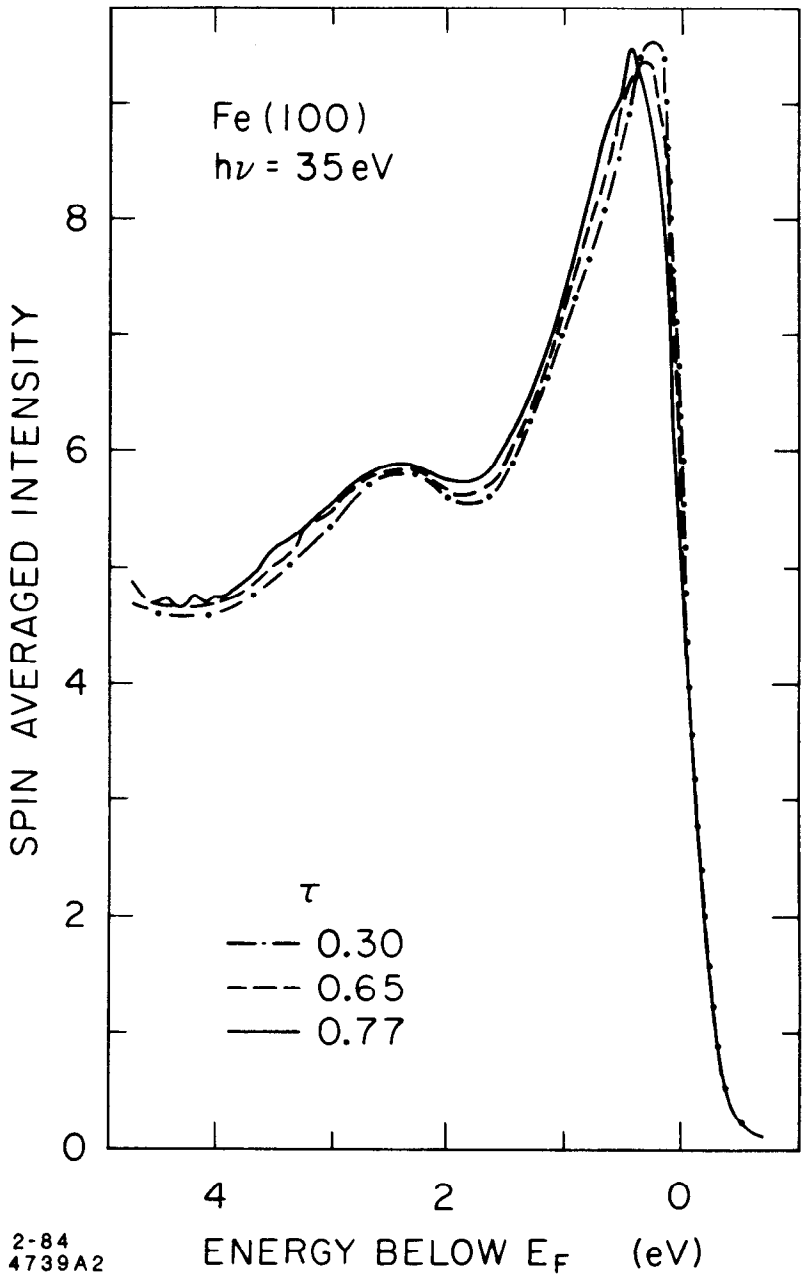
Fe (100)
hν = 35 eV
SPIN AVERAGED INTENSITY
8
6
4
2
0
τ
0.30
0.65
0.77
4
2
0
ENERGY BELOW E_F (eV)
2-84
4739A2

Fig. 15

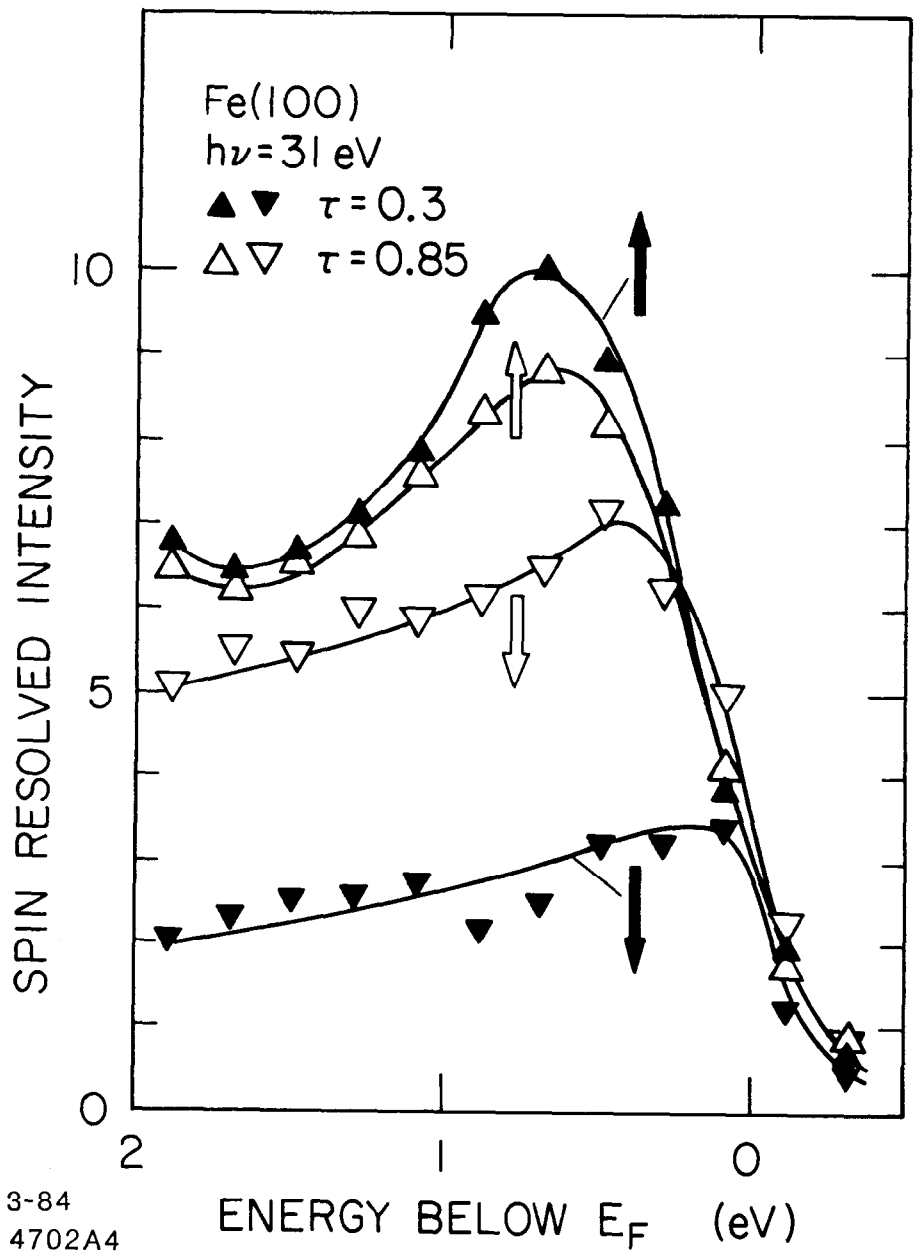
Fe(100)
hν=31 eV
▲▼ τ=0.3
△▽ τ=0.85
10
5
0
2
1
0
SPIN RESOLVED INTENSITY
ENERGY BELOW E_F (eV)
3-84
4702A4

Fig. 16

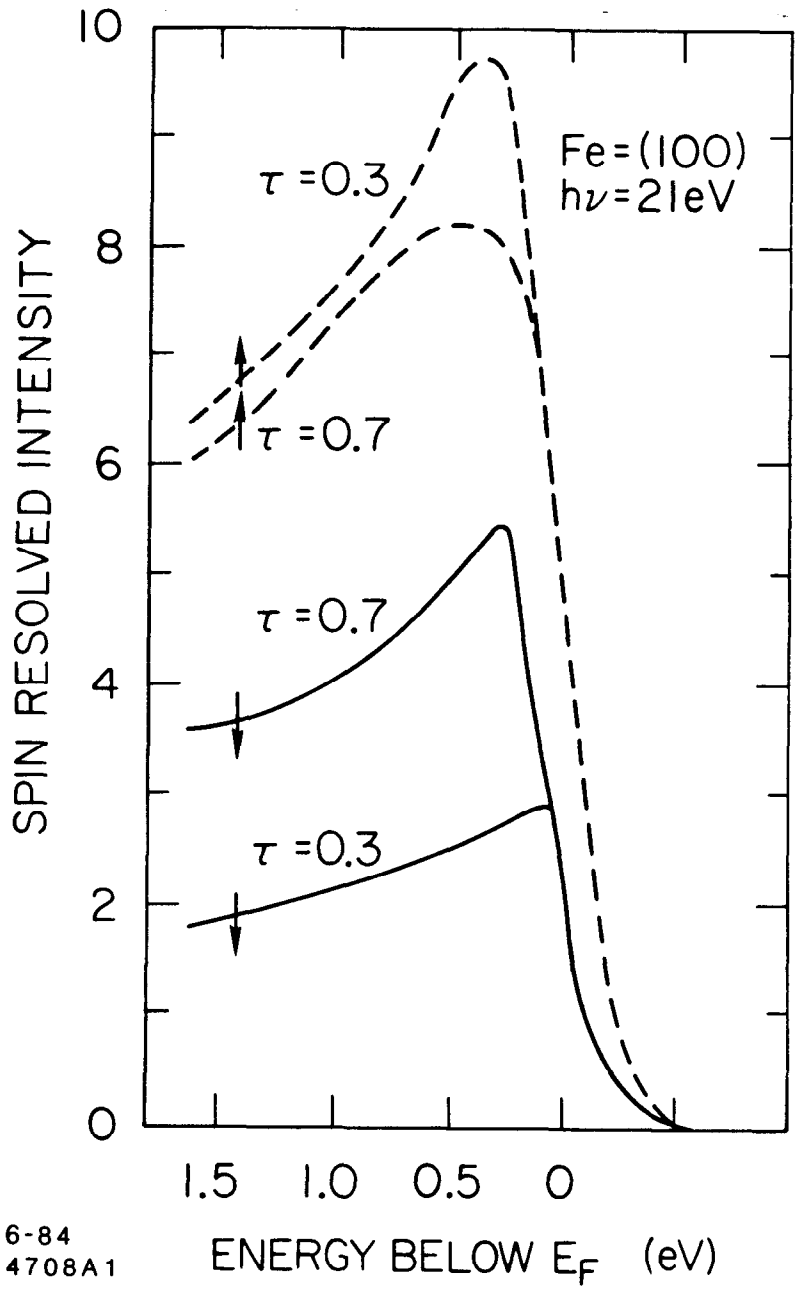
10
8
6
4
2
0
SPIN RESOLVED INTENSITY
τ =0.3
Fe=(100)
hν=21eV
τ =0.7
τ =0.7
τ =0.3
1.5
1.0
0.5
0
ENERGY BELOW E_F (eV)
6-84
4708A1

Fig. 17

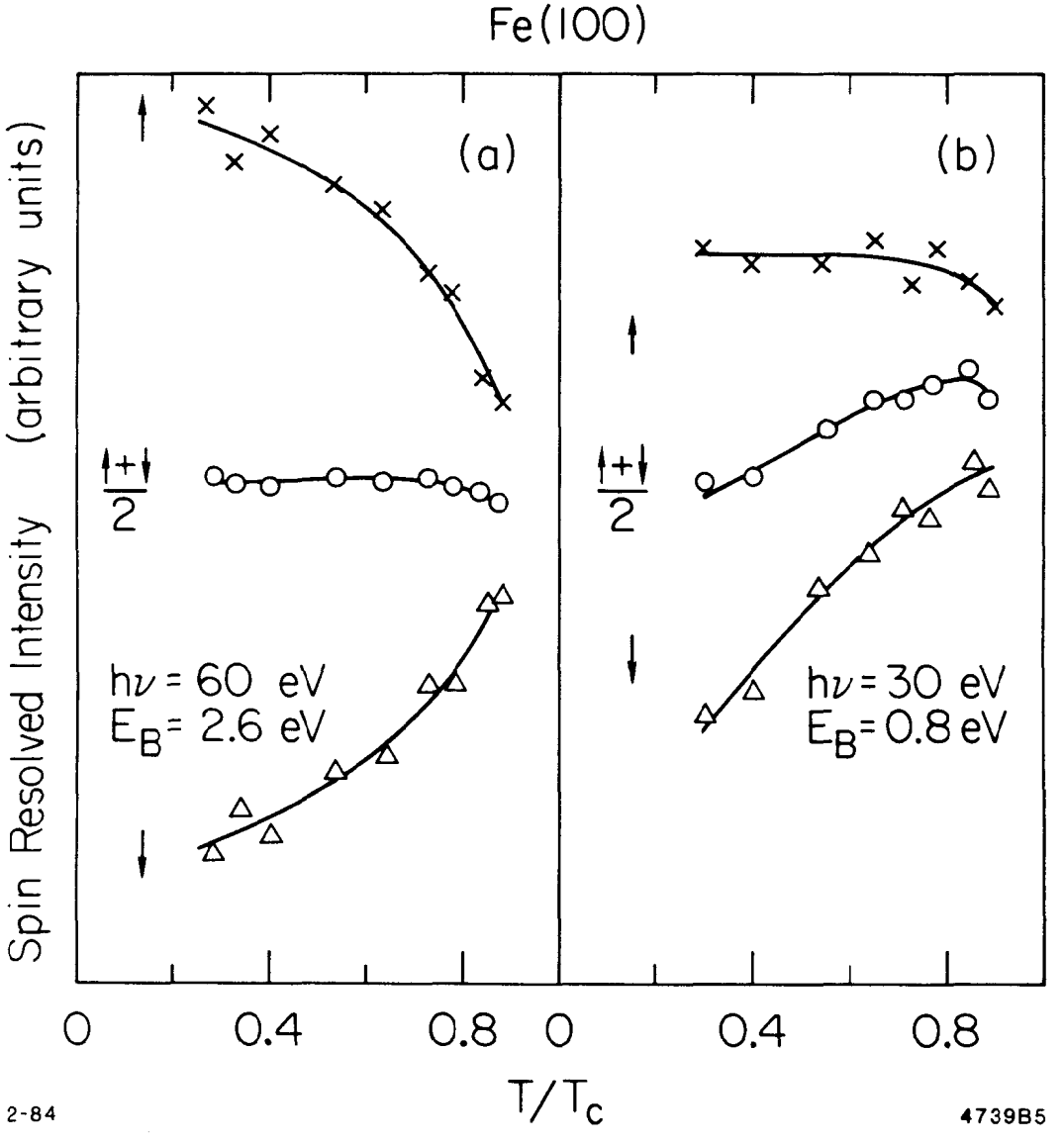
Fe(100)
(a)
(b)
Spin Resolved Intensity (arbitrary units)
↑+↓ / 2
hν = 60 eV
E_B = 2.6 eV
hν = 30 eV
E_B = 0.8 eV
0
0.4
0.8
T/T_c
2-84
4739B5

Fig. 18

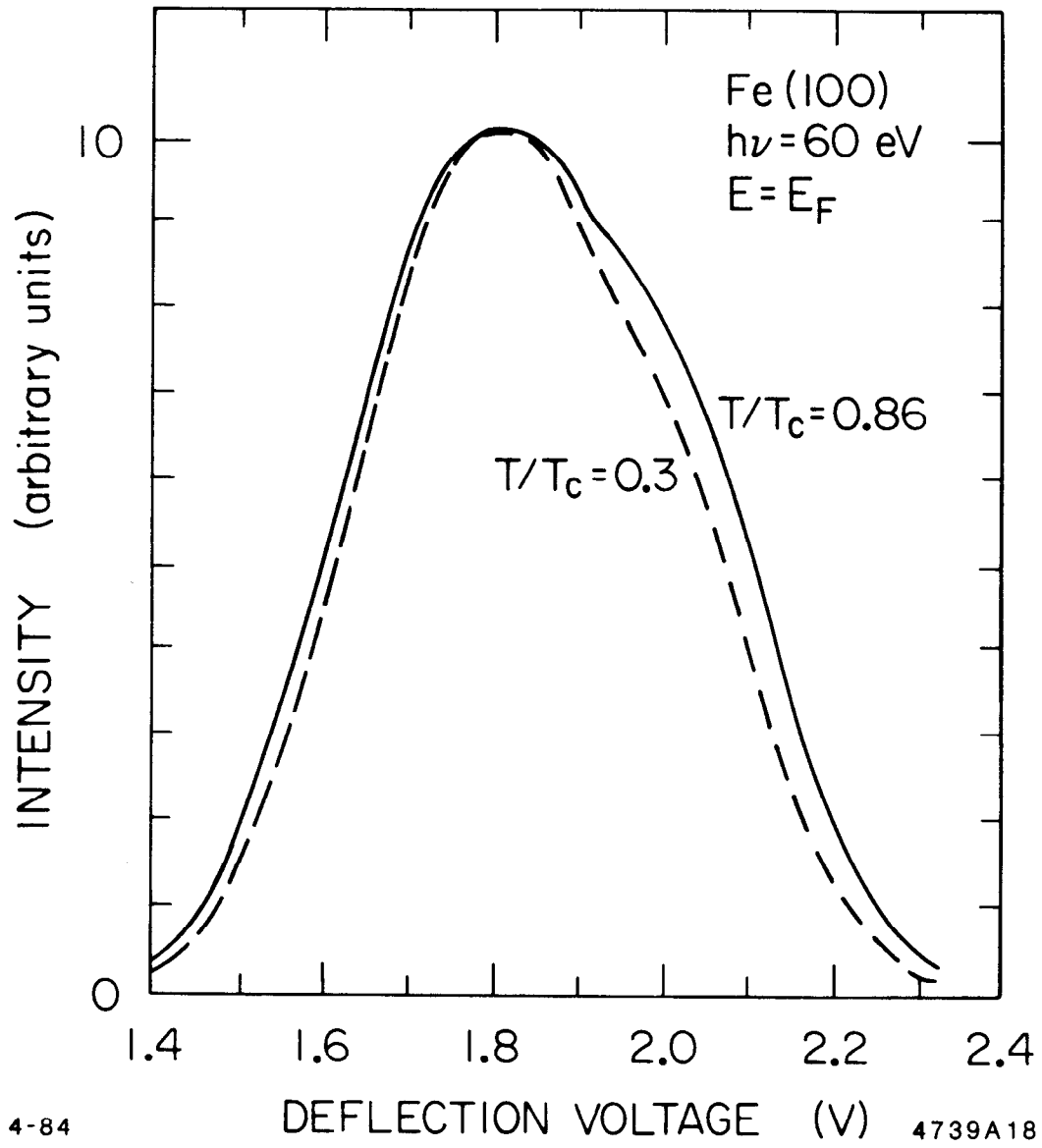
Fe (100)
hν = 60 eV
E = E_F
T/T_c = 0.86
T/T_c = 0.3
10
0
INTENSITY (arbitrary units)
1.4
1.6
1.8
2.0
2.2
2.4
DEFLECTION VOLTAGE (V)
4-84
4739A18

Fig. 19

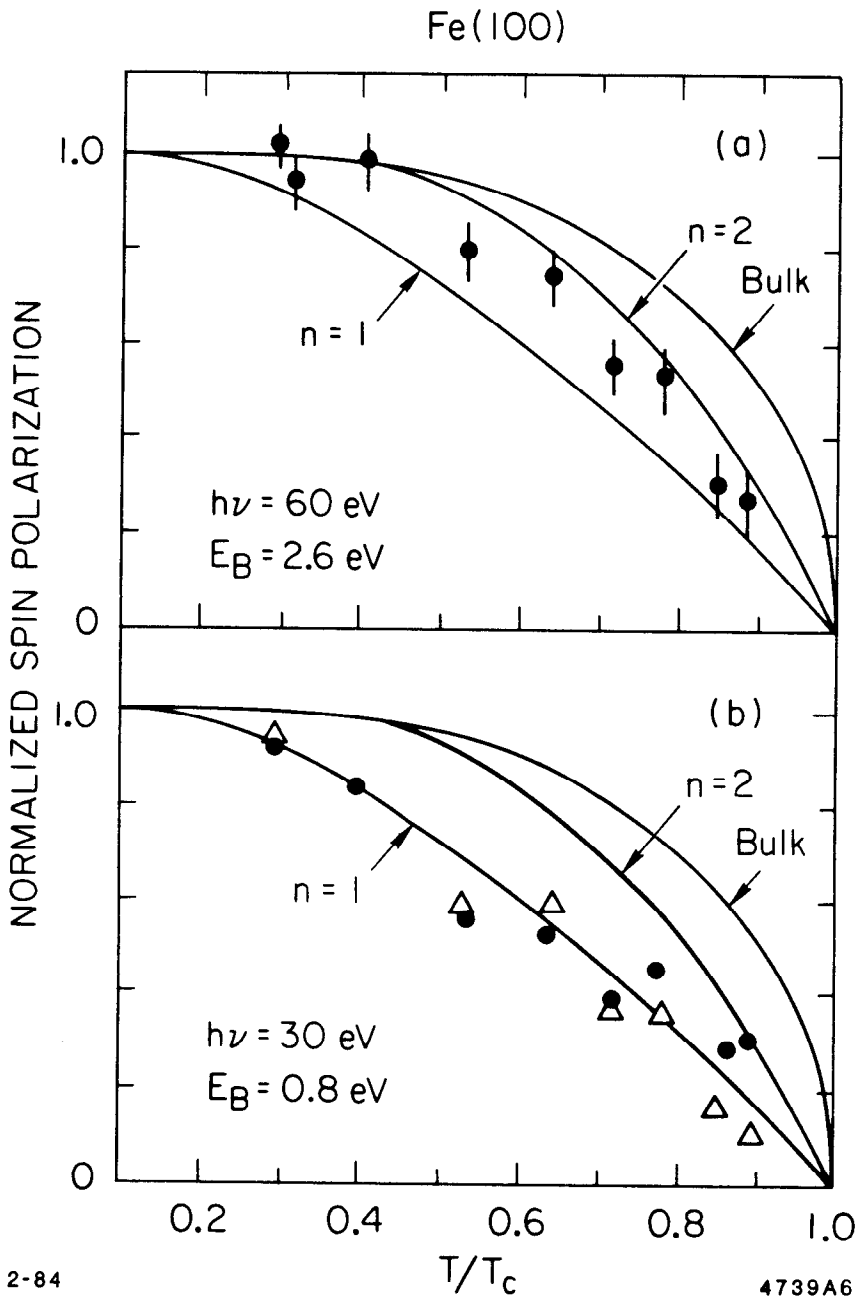
Fe(100)
(a)
n = 2
Bulk
n = 1
hν = 60 eV
E_B = 2.6 eV
(b)
n = 2
Bulk
n = 1
hν = 30 eV
E_B = 0.8 eV
1.0
0
1.0
0
NORMALIZED SPIN POLARIZATION
0.2
0.4
0.6
0.8
1.0
T/T_c
2-84
4739A6

Fig. 20